Precision Measurement of the Mass of the Top Quark in pp̄ Collisions

by

Carlos A. Garcia

Submitted in Partial Fulfillment

of the

Requirements for the Degree

Doctor of Philosophy

Supervised by

Professor Thomas Ferbel

Department of Physics and Astronomy

The College

Arts and Sciences

University of Rochester

Rochester, New York

2007

Curriculum Vitae

The author was born in Buenos Aires, Argentina in February 1976. He graduated from the Instituto Balseiro at Bariloche, Argentina with a Master of Science degree in 2002. He came to the University of Rochester in the fall of 2002 to continue his studies in the field of elementary particle physics. He joined the DØ experiment at Fermi National Accelerator Laboratory, where he first worked on the design and development of fast and highly sensitive electronic readout modules for photon counters, and then he conducted the research for his Ph.D. thesis on the top quark under the supervision of Prof. Thomas Ferbel.

Acknowledgments

First, I thank my advisor Tom Ferbel for his support, his insightful questioning of all my steps and his availability in handling the vicissitudes of life on the professional as well as personal level. He helped me mature not only as a scientist but also as human being.

Other individuals have contributed mightily to my education as a scientist. I point in particular to Juan Estrada, Regina Demina and Gaston Gutierrez, who were always willing to devote their time to listen to my questions and proposals, and help sharpen my thinking and guide me through the subtleties of my analysis.

Many more have worked directly in helping me untangle technical issues and shared part of the work load this research demanded. I especially wish to thank Mike Wang and members of the Top-Mass Group with whom I collaborated closely to produce this result, and my colleagues from the University of Rochester and the leaders of the Top Group at the DØ experiment.

Of course, family and friends played an essential role in assuring the success of this enterprise. Without their support and understanding, this road would have likely been too hard to complete on my own. I thank all my good friends and family members who shared either at long distance or at close quarters the good, bad and beautiful moments of these past years.

I recognize the extraordinary opportunity that doing research at the Tevatron accelerator represents, and I thank the Department of Energy for supporting the research of the University of Rochester Group at Fermilab. Finally, I thank Barbara Warren for her great help in dealing with administrative matters at the University.

Carlos

Abstract

We report a measurement of the mass of the top quark (m_{top}) in $p\bar{p}$ collisions at a center of mass energy of 1.96 TeV. The analysis is based on $p\bar{p} \rightarrow t\bar{t} \rightarrow lepton+$jets data recorded with the DØ detector at the Fermilab Tevatron Collider. Events were preselected in the $e+$jets (913 events/pb of data) and in the $\mu+$jets (871 events/pb of data) channels. These were analyzed through a comparison of the matrix element for the production and decay of the $t\bar{t}$ states with data, using a likelihood method and "tagged" b quarks from the $t \rightarrow Wb$ decays. The result yields

$$m_{\text{top}} \;\; = \;\; 170.5 \pm 2.4(stat + \text{JES}) \pm 1.2(syst.) \,\text{GeV},$$

and corresponds to the most precise measurement of m_{top} obtained at the DØ experiment to date. Combining in quadrature the statistical (stat) uncertainties and correlated contributions from uncertainties in the scale for jet energies (JES) with other estimated systematic uncertainties, yields

$$m_{\text{top}} \;\; = \;\; 170.5 \pm 2.7 \,\text{GeV},$$

This improved measurement will help restrict further the range of mass values of the Higgs boson expected in the standard model.

Contents

List of Figures

List of Tables

Chapter 1

Introduction

The top quark was discovered in 1995 at Fermilab during Run I of the Tevatron [1, 2, 3]. Its observation strongly confirmed the veracity of the standard model (SM), the most inclusive and predictive theory in particle physics. However, we still have a tremendous number of questions about the nature of the top quark. Such as, why is it so massive compared to the other quarks? Is its charge and spin consistent with predictions of the SM? What is its lifetime and what are its decay modes? Moreover, because of its large mass, it has been argued that a better understanding of the top quark will help provide insight on the physics that lies beyond the SM. For example, the mass of the top quark along with the mass of the W boson constrain the mass of the hypothetical Higgs boson [4]. The origin of electroweak symmetry breaking, as exemplified by the difference in the mass of the photon and the W and Z bosons, is now the most important issue in particle physics that the properties of the top quark might shed light upon.

The thirst for an ever deeper understanding of nature is the unmistakable mark of science. After the discovery of the final quark of the SM, it became crucial to measure its properties, and especially its mass to high precision ($< 1\%$ uncertainty

in the top-quark mass). This kind of precision requires the develpment of highly sophisticated methods of analysis. At the Tevatron, the statistics on $t\bar{t}$ events are limited, and therefore a very sharp and meticulous procedure is required to minimize both the systematic and statistical uncertainties of the measurement.

The emphasis of this thesis is both on the measuring technique and the corresponding result extracted from the data collected in the DØ detector located at Fermilab during Run II of the Tevatron. The $t\bar{t}$ events were produced in $p\bar{p}$ collisions at a center of mass of $\sqrt{s} = 1.96$ TeV.

The theoretical motivation for the analysis is given in Chapter 2. A description of the Tevatron Collider and the DØ detector is contained in Chapter 3. Issues in event reconstruction and object identification are discussed in Chapter 4. Selection criteria used in this analysis are given in Chapter 5 and details of the analysis in Chapter 6. The measurement of the mass of the top quark is presented in Chapter 7. A summary and conclusion is provided in Chapter 8. The Appendix contains a brief study of the optimization of the neural network (NN) for selecting b-jets that should be useful the future applications of the method developed in this thesis.

Chapter 2

Theoretical Aspects

2.1 The Standard Model

The top quark was the last expected member of the family of quarks that constitutes part of the standard model (SM) of particles and fields [5, 6]. When the top quark was discovered at Fermilab in 1995, the SM was shown once more to be a reliably predictive theory, despite that it does not offer an explanation for the different particles nor their masses. The quarks (q) and leptons (ℓ) that constitute all the matter of the SM are given in Table 2.1. These fundamental objects differ in their electric charge and in their "flavor" (e.g., strangeness or charm) content, but all have spin $J = 1/2$ [7].

The first generation of particles forms the building blocks of all the matter that characterizes the visible parts of the universe. For each particle in the SM, there is also an antiparticle with opposite quantum numbers (like charge and flavor), and these antiquarks and antileptons define the antimatter of the SM.

The SM also contains particles that provide interaction among the matter particles. There are four known fundamental forces in nature, the strong, the elec-

	The Three Generations		
	I	II	III
leptons:	ν_e (1953)	ν_μ (1962)	ν_τ (2000)
	e (1897)	μ (1936)	τ (1975)
quarks:	u (1964)	c (1974)	t (1995)
	d (1964)	s (1964)	b (1977)

Table 2.1: The three generations of the fermionic constituents of matter, with the dates of discovery in parentheses. (1964 marks the introduction of the quark concept by Gell-Mann and Zweig [8, 9].)

tromagnetic, the weak and the gravitational interactions, with gravity not being a part of the SM. The particles that carry the interaction of the forces (mediators) are called gauge bosons. The photon is the gauge boson for the electromagnetic force, with the quantized form referred to as quantum electrodynamics (QED). The gluon is the gauge boson for the strong (or "color") force, known as quantum chromodynamics (QCD). The charged W^+, W^- and the neutral Z are the gauge boson of the weak force. The field theory describing these interactions provides the means to calculate in detail the dynamics of different processes of the fundamental objects of nature, including their self-interactions.

However, although the SM has been successful in describing nearly every observed process in particle physics, many interesting questions are still to be answered. In its theoretical framework, the SM contains only massless particles, and the fact that all the particles have mass can only be assured through a symmetry breaking of the theory. Thus far, the most promising way of doing this is through the introduction of an extra Higgs field, with the Higgs boson as part of the SM [10, 11, 12, 13]. The top quark couples maximally to the Higgs boson, and may therefore play an important role in the mechanism of symmetry breaking through the Higgs field, Consequently, the better we understand the top quark, the better

can we constrain the feasibility of the existence of the Higgs boson.

2.2   The Top Quark

A better understanding of the properties of the top quark can have implications even on theories beyond the SM. A precise measurement of its production cross section constitutes a check of the predictions of the SM, especially in the domain of QCD [14]. Also, $t\bar{t}$ events become a major source of background in searches for new physical phenomena, and it is therefore important to understand top production and decay. At the moment, the Tevatron at Fermilab is the only accelerator in the world where the top quark can be produced and studied directly.

2.2.1   Production of the Top Quark

The production of the top quark in $t\bar{t}$ events, shown in Fig. 2.1, takes place through the "color" interaction of QCD, either via gluon-gluon $(g - g)$ fusion or quark-antiquark $(q - \bar{q})$ annihilation. At the Tevatron, where the collisions are between protons and antiprotons, quark-antiquark annihilation constitutes about 85% of the yield. This is because of the higher momentum carried by quarks inside the proton, compared to that carried typically by gluons. The ratio of contributions to $t\bar{t}$ depends on the center-of-mass energy $(\sqrt{s})$. For the Large Hadron Collider (LHC) being constructed at CERN [15], with collisions between protons at $\sqrt{s} = 14$ GeV, the ratio of contributions from $q\bar{q}$ and gg channels almost inverts.

In this work, we consider only the production channel through quark-antiquark annihilation. The impact of gluon fusion is estimated through a systematic uncertainty on the measurement of m_{top}. For completeness, we mention other channels of top production allowed in the SM. The top can be produced singly via the
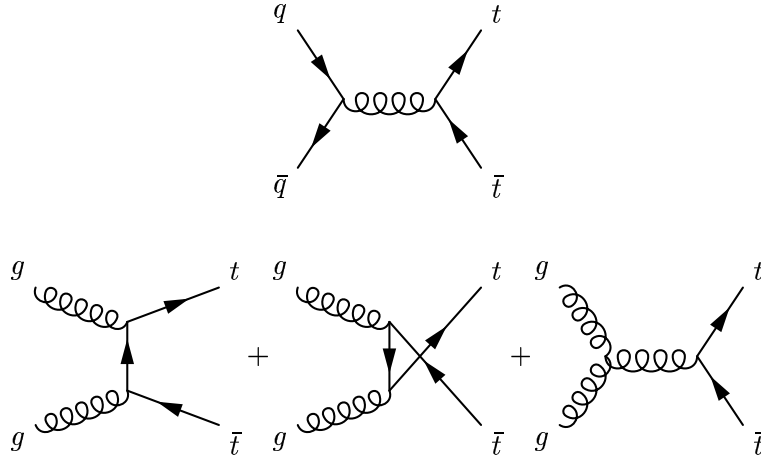
Figure 2.1: Lowest-order Feynman diagrams for the production of $t\bar{t}$ pairs at the Tevatron. At Tevatron energies, quark-antiquark annihilation dominates over gluon-gluon fusion.

electroweak interaction, when a virtual W is produced in a quark-antiquark annihilation and decays in a real top and a b quark. The existence of this important process has been recently confirmed by the DØ collaboration [16].

2.2.2 Top Decay

The top quark is predicted to have a very short lifetime ($\approx 5 \times 10^{-25}s$), and because this scale is about an order of magnitud shorter than the scale for QCD processes, top tends to decay before hadronizing. These characteristics make the direct observation of the top quark impossible. Because quark flavor is violated in the decay, the open channels for decay of the top quark in the SM are through the weak interactions. In the SM, the top quark decays into a W and a b quark, with a branching > 0.998, according to the electroweak vertex described in the Expression 2.1, where $|V_{tb}|^2 \approx 1$, and V_{tb} corresponds to the Cabibbo-Kobayashi-Maskawa matrix element for the $W \rightarrow tb$ transition[17]:

$$\frac{-ig}{2\sqrt{2}} \; \bar{t} \; \gamma^\mu \; (1 \; - \; \gamma^5) \; V_{tb} \; b \; W_\mu \tag{2.1}$$

where g is the electroweak coupling constant, $\bar{t}$ and b correspond to the antitop quark and b-quark spinors. W_μ is the charged vector field and the γ are the standard Dirac Matrices. At leading order in weak interactions, and assuming the b-quark massless, the width of the top is given by [7]:

$$\Gamma_t \;\; = \;\; \frac{G_F m_t^3}{8\pi\sqrt{2}} \left(1 - \frac{m_W^2}{m_t^2}\right)^2 \left(1 + 2\frac{m_W^2}{m_t^2}\right) \left[1 - \frac{2\alpha_s}{3\pi}\left(\frac{2\pi^2}{3} - \frac{5}{2}\right)\right]$$

$$\approx \;\; 1.50 \text{ GeV} \;, \text{ for } m_t = 175.0 \text{ GeV} . \tag{2.2}$$

where G_F is the Fermi weak coupling constant ($g^4 = 32G_F^2 m_W$), m_W is the W mass, and α_s is related to the strong coupling constant $g_s = 4\pi\alpha_s$. The top quark can also decay into a W and an s or d quark. In addition, top can decay through flavor-changing neutral currents, such as $t \to q\gamma$ and $t \to qZ$, but with very low probability. Beyond the SM (e.g. in Supersymmetry), top could decay to a charged Higgs ($t \to H^+ b$). In our work, we assume that top decays to a W and a b quark.

The b-quark, with a long lifetime ($\approx 1.45ps$), hadronizes to form a jet of particles before decaying. Such jets of particles correspond to the physical remnants of the QCD colored quarks and gluons. This characteristic of the b-quark is exploited in the algorithms used to indentify b-quark jets, as it will be discussed later in the thesis, when we differentiate b jets from light quarks and gluon jets. The W boson decays into a lepton-antilepton or quark-antiquark pair. To good approximation (assuming the mass of the fermions $m_f = 0$), the decay to any pair of quarks of sufficiently low mass can take place through any of the three color configurations,

or through any allowed lepton-neutrino pairs, and are all equally likely (W decay to $t\bar{b}$ is forbidden by energy conservation). Figure 2.2 shows the different final states allowed for $t\bar{t}$ events, and their relative probabilities. From this chart, we
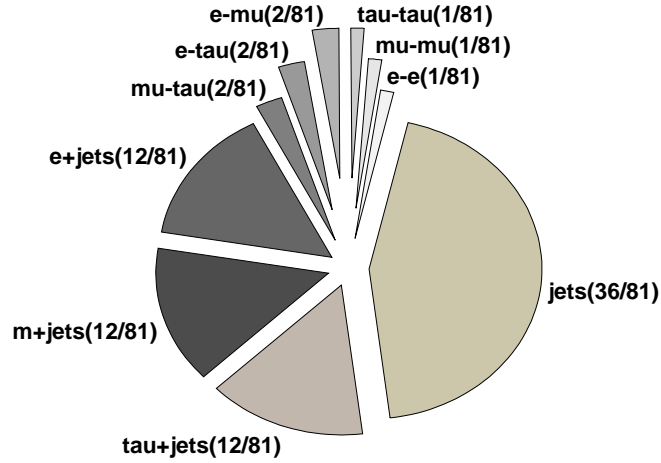
Figure 2.2: Allowed $t\bar{t}$ event-decay channels, and their approximate rates given in brackets.

see that there are three main signatures for $t\bar{t}$ final states: all jets, ℓ+jets and $\ell\ell$+jets. In this work, we consider final states that contain an electron or a muon and four jets, two from b-quarks and two from one of the W bosons that decays to hadronic jets.

2.3 The b Quark

The b quark has particular characteristics that make it possible to differentiate its hadronization products from those of a light quark or a gluon. It hadronizes promptly, leading to a B hadron (often a B meson) and other remnants. The B particles have typical lifetime of ≈ 1.6ps, and can travel several millimeters from

the primary vertex before decaying. In the spectator model, the lifetime of the B hadron depends only on the properties of the b quark, thereby predicting all B mesons to have similar decay lengths [7]. B-hadron decays have relatively high particle multiplicity, and large leptonic branching ratios of about 10%. On the other hand, light quarks and gluons hadronize promptly, mostly into neutral and charged pions.

Thus $t\bar{t}$ events have two b quarks in the final state. These two quarks provide an important differentiation of $t\bar{t}$ relative to the main background, which consists of a W boson and light jets in the final state.

2.4 W-Boson Production

As mentioned before, the production of W bosons in association with extra jets is the main source of background for the top-mass measurement in the lepton + jets channel. Figure 2.3 shows the Feynman diagrams for such events, which are produced through the electroweak interaction in association with two jets generated through the strong QCD color interaction.

The number of contributing diagrams increases rapidly with the number of partons (i.e., quarks and gluons), but with $\alpha_s \approx 0.1$, the yield decreases strongly with number, at least for lower orders [14]. Fortunatelly, there are differences in kinematics for these processes compared to top-pair production. The jets produced in association with the electroweak W boson originate mainly from QCD bremsstrahlung, which tends to yield forward jets of small transverse momentum (p_T). Also, W bosons from top decay are on average more central than the electroweak-produced single W bosons. In addition, the W bosons from top decay do not have a forward/backward charged asymmetry along the $p\bar{p}$ collision axis that characterizes direct W production. (This asymmetry is due to the fact that
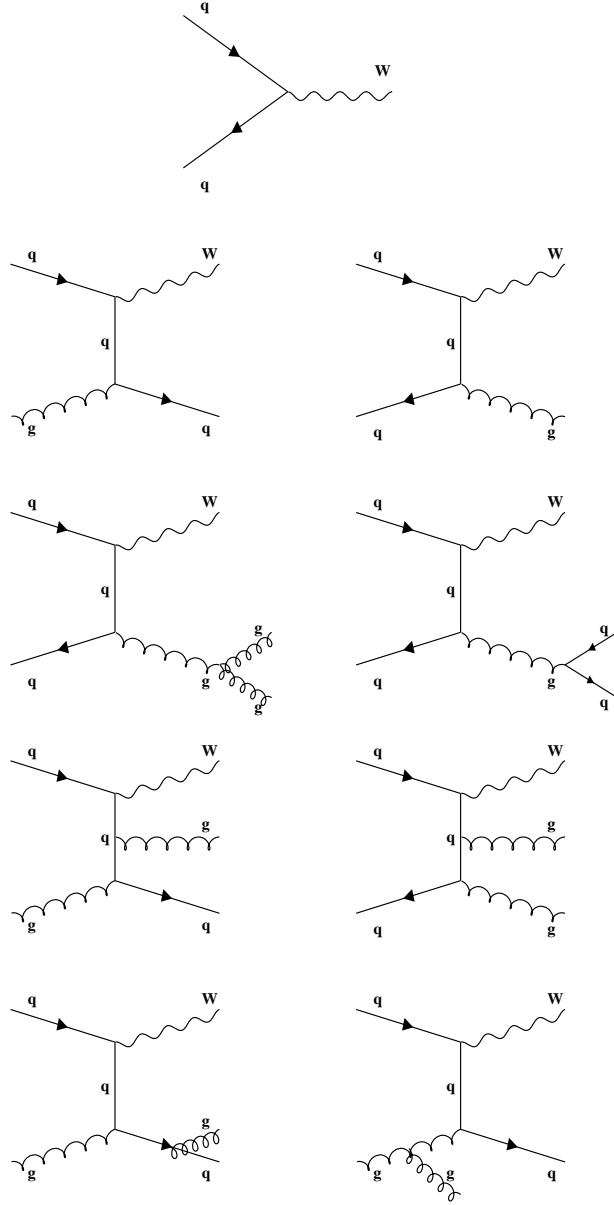
Figure 2.3: Examples of Feynman diagrams for $W+ < 3$ - parton processes.

valence u quarks carry more momentum than d quarks inside protons and antiprotons, and the W^+ is therefore more likely to be boosted along the direction of the proton, and the W^- along the direcon of the antiproton). All these properties affect the lepton products from W decay, making the leptons from $t\bar{t}$ events more central than in direct W production.

2.5   Multijet Production

Multijet events constitute the next important background to our measurement. As in W + jets, multiple jets can be produced through the strong QCD interaction, i.e., through gluon emission and gluon splitting to $q\bar{q}$. In the electron channel, jet characteristics can fluctuate sufficiently to make jets mimic electrons, and thereby introduce background to $t\bar{t}$ signal. The muon channel of $t\bar{t}$ can be mimicked by semileptonic decay of b or c quarks, where the remaining jet has too little energy to be reconstructed efficiently and the muon can appear to be isolated, just as in the case of $t\bar{t}$ events. An apparent imbalance in transverse momentum in the event, usually refered to as $\not{E}_T$, can be caused by escaping neutrinos or through mismeasurement of events. A large $\not{E}_T$ is required in $t\bar{t}$ events, which is meant to signal the $W \to \ell + \bar{\nu}$ decay.

2.6   Other Processes

Other contributions to background arise from single-top production, vector-boson pair-production and production of $\tau^+\tau^-$ pairs. However, these contributions are small compared to the two previously mentioned backgrounds and are ignored in this study.

Chapter 3

Experimental Facilities

This thesis involves an analysis of data collected at the DØ detector, using beams of protons and antiprotons colliding head-on at a center of mass energy of 1.96 TeV. The source of these powerful beams is a huge accelerator complex at Fermilab consisting of a series of consecutive accelerators, with the Tevatron as its final stage. In this chapter, we present a brief description of the accelerator chain and provide an overview of the DØ detector.

3.1   The Accelerator Complex

Several stages of acceleration are needed to reach the 1.96 TeV energy for collisions of protons and antiprotons at the Tevatron, which is currently the most powerful accelerator in the world [18].

The Pre-Accelerator, Linac and Booster

Everything starts at a Cockroft-Walton pre-accelerator that generates H^- ions with 750 KeV of kinetic energy. These ions are fed into the linear accelerator

(Linac) in bunches at a rate of 201.24 MHz.

The Linac accelerates the H^- ions to 400 MeV using the electric field in RF cavities that extend for 150 m. These bunches of accelerated H^- ions are then injected into the Booster.

The Booster is a circular synchrotron 151 m in diameter. At injection, the H^- ions are stripped of their electrons by passing them through a thin carbon foil. The protons are then accelerated to 8 GeV and passed to the Main Injector.

The Main Injector is also a circular synchrotron with a diameter of 1 km, where protons from the Booster are accelerated from 8 GeV to 150 GeV. Antiprotons, produced by 120 GeV protons at the Antiproton Source (see below) are focused, retuned and accelerated from 8 GeV to 150 GeV in the Main Injector. (The Main Injector provides the 120 GeV protons to the Antiproton Source, which is used to produce and collect 8 GeV antiprotons.)

The Antiproton Source

The 120 GeV protons from the Main Injector impact a nickel target at the Antiproton Source. The produced particles include antiprotons, with an efficiency of one antiproton of 8 GeV per $\approx$ 50,000 incident protons (after focusing and filtering). To provide good bunches for collisions in the Tevatron, the antiproton beam has to be reduced in its transverse-momentum phase space. This process is called stochastic "cooling", after which bunches of well focused antiprotons are transfered to the Main Injector to be accelerated to 150 GeV.

Tevatron

The Tevatron is the final stage of acceleration. This synchrotron accelerator ring has a diameter of $\approx$2 km, and uses superconducting magnets of up to $\approx$4 Tesla to

bend and contain the beam. The 150 GeV protons and antiprotons are accelerated to 980 GeV in opposite directions, leading to 1.96 TeV collision energy in the center of mass. A total of 36 bunches of protons and 36 bunches of antiprotons share the same pipe and travel in opposite directions. Each proton bunch carries roughly 3×10^{11} protons, and the antiproton bunches carry $\approx 3 \times 10^{10}$ antiprotons. These bunches collide at two points of the ring (DØ and CDF) with a design frequency of one collision every 396 ns.

3.2　The DØ Detector

Given the broad range of analyses that can be performed at DØ, the detector was designed as a multipurpose device [19]. It can be considered as a combination of three major components, the charged-particle tracking system, the calorimeter and the muon detector. Figure 3.1 shows a sketch of the DØ detector [20].

The Coordinate System

The coordinate system is defined with the z axis along the beam pipe, with the positive direction pointing along the motion of the incident protons. The y axis points upwards and the x axis towards the center of the Tevatron ring, forming a right handed coordinate system. The center of the detector defines the origin of the "detector coordinate system" (or det). Another important coordinate system is the "interaction coordinate system", defined by the origin of the point of the $p\bar{p}$ interaction.

In addition to the Cartesian system, a reformulation of the (r, θ, ϕ) cylindrical coordinate system is very useful. The polar angle for any emitted object $\theta = \arccos \frac{z}{\sqrt{x^2+y^2+z^2}}$ defines the pseudorapidity η:

Forward Mini-drift chambers

Central Scintillator

Forward Scintillator

Shielding

New Solenoid, Tracking System Si, SciFi,Preshowers

NORTH

SOUTH

MUON IAROCCI PLANES

MUON TOROID

MUON TRIGGER DETECTORS

MUON PDT

P

P̄

CALORIMETER

TRACKING SYSTEM

PLATFORM

5

0

-5

m) 0

0

5

10

(m)
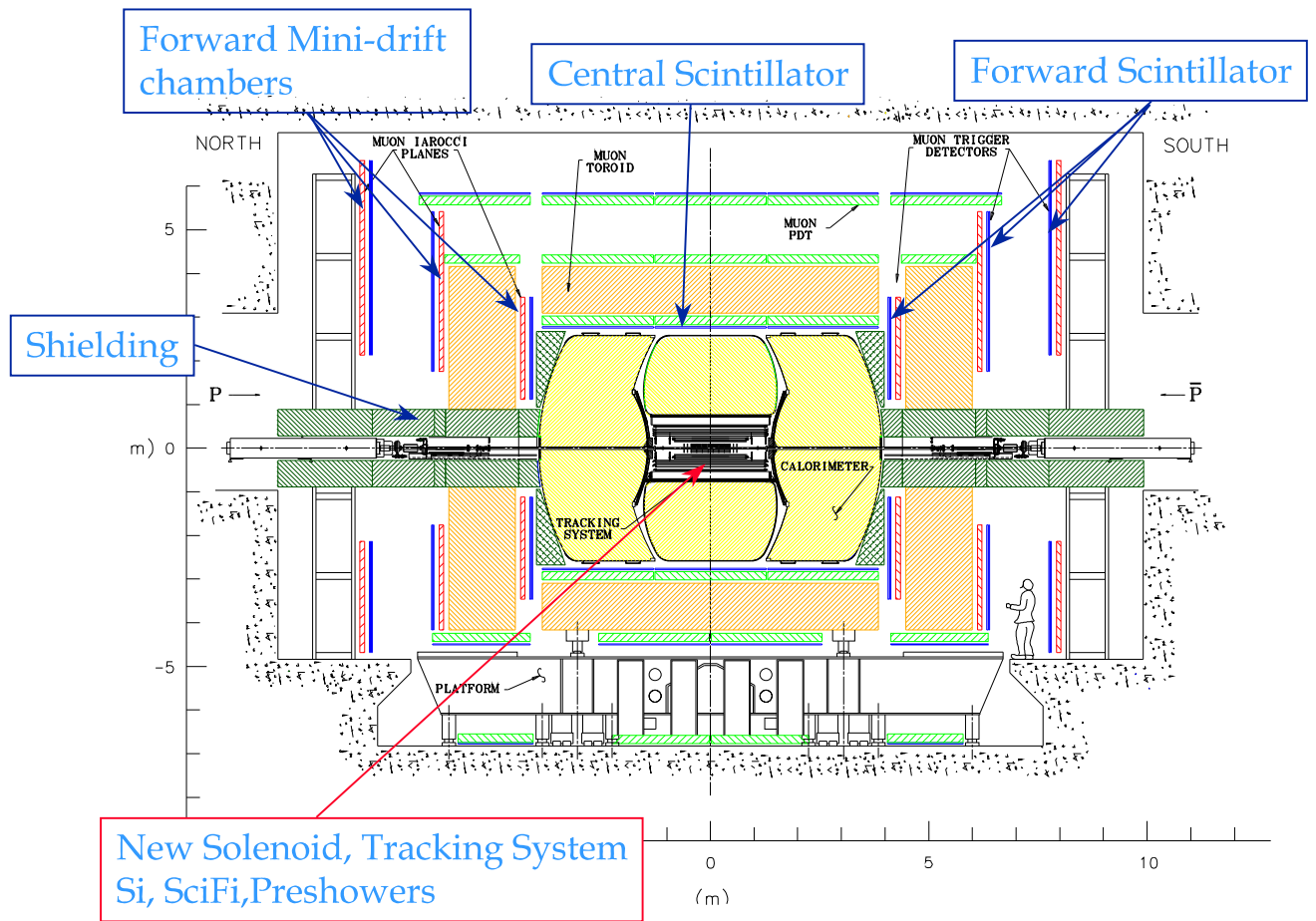
Figure 3.1: Side view of the DØ detector.

$$\eta = -\ln \tan \frac{\theta}{2} . \tag{3.1}$$

The pseudorapidity is an approximation to rapidity $y = \frac{1}{2} \ln \left(\frac{E+p_z}{E-p_z} \right)$, and corresponds to y when particle masses can be neglected within E. Rapidity intervals between two produced objects are invariant to Lorentz-boosts along the z axis. Unless specified to the contrary, references to η in what follows should be taken as calculated relative to the center of the detector. That is, η is normally to be regarded as η_{det}).

3.2.1 The Central Tracking System

The Central Tracking System (CTS) is designed to measure the momentum, direction and electric charge of particles produced in the $p\bar{p}$ collisions. The CTS is enclosed in a $\approx$2T solenoid, with the magnetic field aligned along the z axis such that charged particles are bent in the transverse plane. Hence, the transverse momentum of a particle is obtained from its radius of curvature (r) in the transverse plane.

Silicon Microstrip Tracker

The component of the CTS closest to the beam line is the Silicon Microstrip Tracker (SMT) [19]. The primary goal of the SMT is to provide a high-precision measurement of the primary and secondary interaction vertices. This detector is made of a combination of 6 barrels and 16 disks. The barrel detectors have 4 layers (where each layer has two somewhat overlapping sub-layers) that provide mainly the (r, ϕ) coordinates, and the disk detectors that yield the (r, z) coordinates of

tracks. Figure 3.2 shows a schematic of the SMT. The disks located at the ends are called "H-disks" and the smaller disks in the inner region are called "F-disks". With this arrangement, the SMT provides detection up to $|\eta| = 3.0$

Charged particles passing through the 300μm thick wafers of n-type silicon of the SMT produce pairs of electrons and holes. The charge is collected by strips of p-type or n^+-type silicon. The separation between these strips is normally 50 - 150 μm. The typical axial hit resolution is about 10 μm, and the resolution along the z axis is 35 μ or 145 μm, depending on the stereo angle.
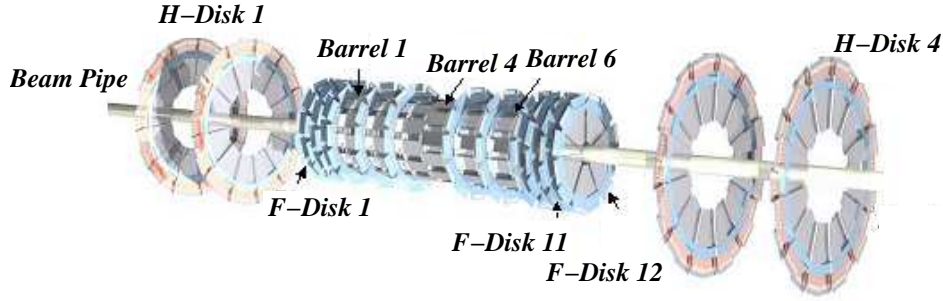
Figure 3.2: Schematic 3D view of the silicon vertex detector.

The Central Fiber Tracker

The Central Fiber Tracker (CFT) [21] is made of 835 μm (diameter) scintillating fibers arranged in 8 double layers on thin carbon-fiber cylinders of radius from 20 to 52 cm. The outer CFT complements the high precision of the inner SMT to provide an overall excellent transverse momentum resolution for charged particles. Each thin cylinder supports an axial layer of fibers and a stereo layer at an angle of 3°. The two inner cylinders are 1.66 m long and the outer six are 2.52 m. The cluster resolution is of $\approx$100 μm per doublet layer. When a charged particle crosses a fiber, the scintillating material inside the fiber produces light at a wave length λ =340 nm, which is absorbed and remitted at λ =530 nm by a wave-shifting

dye. The light then travels to the end of the fiber at the edge of the cylinder, where it is transfered to clear optical fibers. Finally, the clear wave guides carry the light signal to Visible Light Photon Counters (VLPC) that translate the light into electric charge [22]. The VLPCs work at a temperature of 9K and have a high quantum efficiency ($\approx 85\%$). A minimum-ionizing particle produces about eight photons per layer, and the VLPC generates about 30 - 60 k electrons per photon. The aperture of the CFT covers $|\eta| < 3$.

3.2.2   The Calorimeter

The liquid argon calorimeter [23] was designed to measure the energy of electrons, photons and jets. It consists of a central calorimeter (CC), covering roughly $|\eta_{det}| < 1$, and two end calorimeters (EC) to cover the forward regions up to $|\eta_{det}| \approx 4$. Each calorimeter has its own cryostat and consists of two main parts. Closer to the interaction region are the electromagnetic calorimeters, and the outer sections contain fine and coarse hadronic calorimeter modules. The electromagnetic part is designed to absorb most of the energy of entering electrons and photons. The hadronic component of particle showers normally penetrates through the hadronic sections. Layers of passive dense material induce particle showers for any particles traversing the calorimeter. The passive layers alternate with active layers that detect the surviving particles. The active material is always liquid Argon kept at a temperature of $\approx$80K. The passive materials are different for each region. The electromagnetic sections use 3 to 4 mm plates of depleted uranium. The fine hadronic parts use uranium plates 6 mm thick, and the coarse sections use 46.5 mm thick plates of copper in the CC and stainless steel in the EC. Most of the calorimeter is divided into cells of $\Delta\eta \times \Delta\phi = 0.1 \times 0.1$. In the forward sections (with $|\eta| > 3.2$) the cells are about 0.2×0.2. And the third layer of the electromagnetic

calorimeter cells have $\Delta\eta \times \Delta\phi = 0.05 \times 0.05$, to provide increased resolution where the electromagnetic shower is expected to have its maximum number of particles.

Inter Cryostat Detector

Another part of the calorimeter is the inter-cryostat detector ICD [23] that covers the gaps at $0.8 < |\eta| < 1.4$ between the CC and the two EC, thereby improving overall jet-energy resolution. This detector is segmented in scintillating tiles of $\Delta\eta \times \Delta\phi \approx 0.1 \times 0.1$.

Central and Forward Preshower Detectors

Preshower detectors in the central (CPS) and forward (FPS) regions provide better electron and photon identification [24, 25]. The CPS preshower detectors use three layer of triangular scintillator fibers that follow a layer of lead, and are postioned in a gap between the solenoid and the central calorimeter. The FPS components are attached to the faces of the two forward calorimeters, and are composed of a double layer of scintillators, a lead layer, followed by another layer of scintillators. Just as the CFT, both the CPS and the FPS are read out using fibers.

3.2.3 Muon Detector

The muon detection system comprises the outer part of the DØ detector [26, 27]. Muons produced in a hard $p\bar{p}$ scatter usually travel almost undisturbed through the central tracker and the calorimetry.

The muon detector is divided into two sections: a central part for $|\eta| < 1.0$, and forward parts for $1.0 < |\eta| < 2.0$. Trajectories are measured using proportional drift tubes (PDTs) and scintillating pixels and $\approx$1.9 T toroidal magnets [28]. One

of three layers (layer A) is located before the toroid and the other two (layers B and C) are outside of the magnet.

3.2.4   Trigger and DAQ

The Tevatron produces collisions every 396 ns, or at a rate of about 2.5 MHz. However, only a very small fraction (10^{-10}) of these are of interest for our analysis, and, more important, only $\approx 50\ Hz$ can be stored as physical media. Most of the interaction correspond to multijet events. Production of massive particles such as W or Z bosons is also rare (10^{-5}), and these we wish to keep. (Production of b quarks is at $\approx 10^{-3}$ level.)

Offline reconstruction capabilities define a limit of ≈ 50 Hz on the events that are collected. A three-stage trigger system is therefore used to reduce data from the overwhelming 2.5 MHz to the 50 Hz rate. The higher levels fo the trigger analyze the data in greater detail, applying consecutively more restrictive requirements [29]. The trigger rejects most of the uninteresting events, but also interesting ones resulting from trigger inefficiency or because the system is busy reading a previous event ("dead time").

The first level of the trigger (Level 1) is a hardware trigger that receives fast input selected using the luminosity monitor[30], the calorimeter and muon detectors. It analyzes data at a rate of 2 KHz. It seeks collisions that have z positions well within the DØ detector, checks that the energy deposited in the calorimeter is beyond some minimum threshold, and triggers the presence of muons.

The Level-2 trigger is also a hardware system that reduces the data rate to 1 kHz, taking into consideration correlations among sub-detector outputs.

The final trigger stage is Level 3, which uses about 100 CPU farm nodes to provide minimal reconstruction of events. Decisions whether to keep an event

are based on whether objects such as jets, electrons or muons are present. The acceptance rate is then reduced to 50 Hz through variable selection criteria, and all accepted events are then stored for offline reconstruction and analysis.

Chapter 4

Event Reconstruction and Object Identification

The initial signals from any given collision consist of about a million channels of output. A series of reconstruction algorithms take this data and identify any physical objects associated with the event [31]. What follows is a description of the dedicated algorithms used to reconstruct the key objects needed to analyze $t\bar{t}$ events.

4.1   Tracks of Charged Particles

The tracking system in DØ provides a large fraction of the initial signals. To find tracks, the reconstruction algorithm first defines clusters of hits per layer (hit clustering), and runs a fitting sequence (track finding) to trace the most likely path of a hypothesized charged particle. The track-finding sequence is divided into two stages: pattern recognition, to choose the clusters associated with a traversing particle, and a fit to a track using the Kalman Filter [32].

4.2 Primary Vertex

A primary vertex (PV) defines the position of the $p\bar{p}$ collision. The algorithm used to find the primary vertex is the Adaptive Primary Vertex (APV) [33]. The b-tagging algorithm follows, relying on good reconstruction of the primary vertex. The important elements of the APV algorithm can be summarized as:

- All track candidates for a primary vertex are fitted using the Kalman Filter algorithm. Each track is weighted according to its weight function $\omega(\chi^2)$.

$$\omega(\chi_i^2) = \frac{1}{1 + e^{(\chi_i^2 - \chi_{cutoff}^2)/2T}} \tag{4.1}$$

  where χ_i^2 is the contribution to the normalized square of the deviations from track-i to the χ^2 for the fit to any primary vertex, and χ_{cutoff}^2 is the χ_i^2 at which the weight function equals 0.5. T is a parameter that reflects the fall-off of the ω function with χ_i^2. Initially, all track weights are set to 1.0. At iteration k, the weight of a track depends on the distance of closest approach (dca) of the track to the vertex at iteration $k - 1$.

- For each track used in the fit, its weight is re-computed according to the χ^2 for the newly fitted vertex. If $\omega_i(\chi^2) < 10^{-6}$, track-$i$ is eliminated from the fit.

- Above is repeated until the weight for all tracks converges.

The following selections are applied to a primary vertex of an event:

- $|z_{PV}| \leq 60$ cm.

- At least three tracks are fitted to the PV ($Ntrks_{PV} > 3$).

4.3   Muons

Two parts of the detector are used to reconstruct information on muons: (i) the central tracker, which provides precision and confirmation that the muon originated from the primary vertex, and (ii) the outer muon system, where each of the three layers of PDT must have a hit.

The following are the standard Muon ID acceptance requirements:

- $|nseg| = 3$, of medium quality.

  Corresponds to three segments of the muon trajectory reconstructed in the outer muon system. Specifically, using the following Muon ID criteria [34]:

  - At least two PDT wire hits in the A segment,

  - At least one scintillator hit in the A segment,

  - At least two PDT wire hits in the BC segment,

  - At least one scintillator hit in the BC segment.

- Cosmic veto = TRUE.

  A loose criterion is used to reject cosmic rays, This is based on timing information from scintillator hits associated with muons in the A layer and combined BC layers. Scintillator hits must be in time with the interaction: $|t_A| < 10$ ns and $|t_{BC}| < 10$ ns.

- Muon reconstructed $p_T > 20$ GeV.

- Muon pseudorapidity $|\eta| < 2.0$.

- UseCentralMatched = TRUE.

  A central track is required to match a muon in the outer tracker, with additional selection criteria placed on the central track.

- $\chi^2 < 4.0$

  Criterion for the χ^2 for the fit to the central track.

- dcaSignificance < 3.0

  The fitted track should have an acceptable distance of closest approach to the primary vertex.

- DeltaR(muon,jet) > 0.5

  Muons from semileptonic decays of heavy quarks are the main source of background to those from W decays in $t\bar{t}$ events. Isolation is used to distinguish muons from these two sources. A weak isolation criterion defines good candidates by demanding that a muon is separated from any jet, $\Delta R(\mu, jet) > 0.5$ in (η, ϕ) space. The separation between the two classes of muons can be improved further by considering the difference between the p_T spectra of the two sources.

  The addition of this kind of criterion and the ones below defines a "tight" requirement for muons.

- E_T Halo < 0.08 GeV

  Defining the transverse energy (E_T) in a "Halo" region as the sum of the E_T for calorimeter clusters in a ring of radius between $\Delta R = 0.1$ and $\Delta R = 0.4$ relative to the muon axis, an acceptable minimum-ionizing muon is required to have E_T in the Halo of < 0.08 GeV.

- E_T Track < 0.06 GeV

  Defining E_T Track as the sum of the p_T of all tracks within a cone of radius $\Delta R = 0.5$ around the muon axis, not including the track matched to the muon in this sum, an acceptable event requires E_T Track < 0.06 GeV.

4.4   Electrons

Electrons are first identified using calorimetric information. Photons behave similarly in the calorimeter, but they do not have associated tracks that point to energy depositions in the calorimeter. The main challenge in identifying electrons is to minimize confusing them with hadronic jets, which can have fluctuations that can mimic electron signals.

As a first step, a cone algorithm clusters calorimeter cells based on readouts of $E_T >$1.5 GeV in a cone of radius $\Delta R = \sqrt{\Delta\eta^2 + \Delta\phi^2} < 0.2$ relative to the axis of the cells cluster, thereby defining an EM cluster. Parameters used subsequently are calculated for every EM cluster that is formed by the simple-cone algorithm.

The following standard ID requirements are imposed on candidate electrons:

- $p_T > 20 \ GeV$.

- $|\eta| < 1.1$.

- Isolation < 0.15, defined as:

$$EM_{iso} = \frac{E_{tot}(R < 0.4) - E_{EM}(R < 0.2)}{E_{EM}(R < 0.2)}, \qquad (4.2)$$

where $E_{EM}(R < 0.2)$ is the EM energy within a cone of radius $R < 0.2$, and $E_{tot}(R < 0.4)$ is the total (EM + fine and coarse hadronic) energy within a cone of radius $R < 0.4$, both relative to the axis of the candidate electron.

All initial EM clusters are required to have an isolation of < 0.15. The isolation parameter gives a measure of the longitudinal and transverse extent of a given cluster. EM objects tend to deposit most of their energy in a narrow region of the EM layers, while hadrons deposit their energies over a much wider radius, as well as in the hadronic layers .

- EM fraction > 0.90

  This requires that an accepted shower deposits most of its energy in the EM part of the calorimeter. The EM fraction is defined as

  $$EM_f = \frac{E_{EM}(R < 0.2)}{E_{tot}(R < 0.2)}, \qquad (4.3)$$

  where $E_{EM}(R < 0.2)$ is the EM energy within a cone of radius $R < 0.2$, and $E_{tot}(R < 0.2)$ is the total energy within a cone of radius $R < 0.2$.

- $HMx7 < 50$.

  The "H-Matrix" distinguishes between deposition of EM and hadronic energy in a calorimeter by analyzing the longitudinal and transverse shape of a shower. Based on N Monte-Carlo (MC) generated electrons, a covariance matrix (M) is defined using a set of seven discrimination variables:

  $$M_{ij} = \frac{1}{N} \sum_{n=1}^{N} (x_i^n - \langle\, x_i\, \rangle)\, (x_j^n - \langle\, x_j\, \rangle), \qquad (4.4)$$

  where x_i^n is the value of variable i for electron n, and $\langle\, x_i\, \rangle$ is the mean value of variable i.

  Below are the variables used to characterize the 7×7 matrix M:

  - Shower energy fractions in 1st, 2nd, 3rd, and 4th EM layer of the calorimeter.

  - Cluster size in $r - \phi$ based for the 3rd EM layer of the calorimeter (EM showers typically deposit the bulk of their energy in the 3rd EM layer).

  - Total shower energy.

  - Position of the primary vertex for any generated shower.

A H matrix can be defined as the inverse of the covariance matrix M

$$H \equiv M^{-1}. \tag{4.5}$$

Using the H matrix, a χ^2-like variable can be calculated to provide a measure of how likely any observed shower k is consistent with being an EM object originating from its PV.

$$HMx7 = \sum_{ij} (x_i^k - \langle\, x_i\, \rangle)\, H_{ij}\, (x_j^k - \langle\, x_j\, \rangle). \tag{4.6}$$

- TrkMatchChi2P > 0

  A track extrapolated to the calorimeter is required to coincide with the position of energy deposition in the EM calorimeter. A track is considered matched to an EM cluster if the track-matching χ^2 probability is $P(\chi^2) > 0$.

  $$\chi^2 = \left(\frac{\Delta\phi}{\sigma_\phi}\right)^2 + \left(\frac{\Delta z}{\sigma_z}\right)^2, \tag{4.7}$$

  where $\Delta\phi$ (Δz) is the difference in azimuth (in z position) between the EM cluster in the 3rd EM layer and the track extrapolated to that layer. σ_ϕ and σ_z are the root-mean-square values of the experimental resolutions on each quantity.

- Likelihood > 0.85

  A likelihood is used to improve discrimination between electrons and other background objects. This likelihood is based on seven variables, which are described in detail in Ref [36], and defined briefly below:

  - EM fraction .

– H-matrix.

– The ratio of the transverse energy of the cluster in the calorimeter to the transverse momentum of the matched track, E_T^{Cal}/p_T^{trk}. This ratio is a good discriminator since it tends toward 1 for electron signal but not so for background objects.

– The above mentioned track-matching χ^2 probability, $Prob(\chi^2_{SpatialEM-trk})$. Background events tend to have a poor spatial match between a candidate track and calorimeter energy depositions.

– Distance of closest approach of the selected track to a line parallel to the z-axis that passes through the primary vertex.

– Number of tracks in a cone of $\Delta R < 0.05$ about the axis of the candidate electron. This variable is sensitive to photon conversions, since such events have two tracks very close together, rather than just one track expected for a good electron.

– The sum of the p_T of all tracks in a $\Delta R < 0.4$ cone around the associated track. This is intended to remove jets, which tend to have several tracks within this size cone.

4.5   Missing Transverse Energy

Neutrinos cannot be detected in the detector. Their presence is seen indirectly as an imbalance in the momentum in the transverse plane, and referred to as missing transverse energy $\not{E}_T$. A minimum $\not{E}_T$ of 20 GeV is required to accept a $t\bar{t}$ event in the ℓ+jets topology. The three main steps to reconstructing the $\not{E}_T$ are outlined below.

Initial $\not{E}_T$

The imbalance in E_T is formed from the calorimeter readouts associated with all the reconstructed i objects:

$$\Delta E_T|_x = \sum_i E_i sin\theta_i cos\phi_i$$
$$\Delta E_T|_y = \sum_i E_i sin\theta_i sin\phi_i \qquad (4.8)$$

Components of $\not{E}_T$ correspond then to $-\Delta E_T|_x$ and $-\Delta E_T|_y$.

Calorimeter $\not{E}_T$

Since reconstructed jets (see below) and EM objects must be corrected differently in energy, these corrections are used to improve the calculation of $\not{E}_T$.

Corrected $\not{E}_T$

High-energy muons deposite very little of their energy in the calorimeter and this can produce an effective $\not{E}_T$. The energies of muons are reconstructed from the transverse momenta of central tracks that match external muons (reduced by the energy already estimated to have been deposited in the calorimeter). This is used to correct $\not{E}_T$.

4.6 Hadronic Jets

Energy deposited by hadronic objects are reconstructed as jets in the calorimeter, as follows.

The jet reconstruction algorithm associates adjacent clusters of energy in the calorimeter to form jets. The "improved legacy cone" algorithm that we use for

jets of cone size $\Delta R = 0.5$ is described in Ref [37].

Once jets are clustered according to this cone algorithm, additional quality-selection criteria are applied to each jet. The full set of criteria, based on the fractions of EM calorimetric energy (EMF) and the fine and coarse hadronic calorimeter fractions (FHF and CHF), are detailed in Ref. [38], and are designed to remove jets that do not originate from hadronic particles produced in $p\bar{p}$ hard interaction. Additional criteria are needed to select good jets in $t\bar{t}$ events:

- $p_T > 20$ GeV

- $|\eta| < 2.5$

The main source of background to jets are from EM objects and from fluctuations in calorimeter noise.

4.6.1   Jet Energy Scale (JES)

A very important aspect of the reconstruction of a jet in $t\bar{t}$ events is a correction of the reconstracted jet energy to that of the originating parton energy. There are several mechanisms that can cause the energy of the cells clustered into a jet to deviate from the energy of the initial parton. The important ones are listed below [39].

Calorimeter Response (R): Non-linearities and particle-dependent response of the calorimeter can lead to a biased reconstructed energy. Also, during the development of a hadronic shower, some energy is lost to non-ionizing mechanisms that are not detected in the calorimeter (e.g. nuclear break up). Blind spots in some regions of the detector due to faulty electronics or dead material also have to be considered in the calorimeter response.

Energy Offset (O): Signal from the nderlying event (corresponding to "spectator" particles from the break up of the incident p and $\bar{p}$ that do not originate from the hard scatter), multiple interactions, energy pile-up from previous collisions, electronics noise and noise from radioactive emanations from the uranium absorber can provide offsets in observed energies that affect the reconstructed energies of jets, and require rescaling.

Showering Corrections (S): The size of the cone defining a jet is finite, and some particles from the shower are not considered in the clustering of a jet.

Jet Energy Scale (JES) corrections attempt to correct the reconstructed jet energy (E^{reco}) back to the particle-level energy (E^{corr}) namely to the particle fragments of partons before the physical particles interact within the calorimeter. The correction can be written as

$$E^{corr} = \frac{E^{reco} - O}{R \times S},$$

where R is the ratio of the energy response of the calorimeter to the energy of a jet, O is the energy offset, and S is the fraction of a jet's shower that leaks outside the specified jet cone in the calorimeter. Since not all of these effects can be modeled accurately through simulations, a separate JES correction is provided for data and MC by the Jet Energy Scale Group [39]. The current analysis uses the JetCorr v7.1 package [40], with the total systematic uncertainty assigned to the JES correction given by:

$$\sigma = \sqrt{\sigma^2_{stat,data} + \sigma^2_{syst,data} + \sigma^2_{stat,MC} + \sigma^2_{syst,MC}}. \tag{4.9}$$

No special JES correction was applied to jets assumed to originate from a b and c flavor partons, unless soft muons were matched to the jet remnants. In the

latter case, the muon was assumed to originate from semileptonic b decay, and was treated somewhat differently in our analysis, as described later. A more detailed JES correction for jets of heavy flavor is currently being developed at DØ.

4.7   Identification of b Jets

A $t\bar{t}$ event has two b partons. The possibility of identifying (or tagging) b jets reduces the ambiguity in the number of ways of assigning observed jets to specific decay partons. As will be shown in next chapter, this has important impact in our analysis.

There are three main ways to identify a b-jet.

1. Explicitly reconstruct secondary vertices from their charged particle tracks.

2. Identify charged-particle tracks that have large impact parameters (significant dca) relative to the primary vertex.

3. Identify a muon from semileptonic b decay (10% of the time) that is produced within a jet.

A neural network algorithm (NN) developed at DØ to identify b quarks [41, 42] uses input variables that are the outcomes of different taggers. The taggers used as inputs for the NN are the Counting Signed Impact Parameters (CSIP) [43], the Jet Lifetime Probability Tagger (JLIP) [44], and the Secondary Vertex Tagging (SVT) [45], and are based on the three approaches mentioned above.

Tag-Rate Functions (TRF) and Operating Points

The NN algorithm also provides the TRF, which are parameterizations of b-tagging efficiencies as functions of jet p_T and η. The TRF provide an estimate of the

probability for any jet to be tagged, and this probability is used to weight the different permutations of jets assigned to partons, as is described in Chapter 6.

The TRF are derived for three types of jets: light jets, c jets and b jets. TRF also provides result for several different operating points or NN cutoffs in the continuous output of the NN algorithm.

The b-tagging algorithm returns a number between 0 and 1 per jet. An output value close to 1 indicates a high probability for any jet being a b jet. We use the "Medium" operating point, which corresponds to the NN output of > 0.65 to define a b-tagged jet. Several possible operating points with their cutoff values are shown in Table 4.1

Operating Point	Cutoff Value
L6	0.1
L5	0.15
L4	0.20
L3	0.25
L2	0.375
Losse	0.45
OldLoose	0.5
Medium	0.65
Tight	0.775
VeryTight	0.85
UltraTight	0.9
MegaTight	0.925

Table 4.1: Possible operationg points for the NN b-tagger

"Medium" corresponds to the minimum NN cutoff approved by DØ at this time. Reducing this cutoff would provide more b-tagged jets, but would also increase the chances of accepting misidentified jets. Increasing the NN cutoff reduces the mistag rate, but decreases the acceptance for true b jets. A study of the impact of the choice of operating point on the uncertainty in the measurement of m_{top} is presented in Appendix A.

Chapter 5

Data Sample and Simulation

This chapter describes the MC samples used for simulating the data, and for validating and calibrating the method of analysis, and also provides the selections used for the final data sample.

5.1 Monte Carlo Used for Simulation

Physics objects and the details of generated MC samples of ℓ+jets $t\bar{t}$ events [46] and their b-tagging aspects [47] describe quite accurately the broad features of the data.

The PYTHIA program [48] was used to simulate $t\bar{t}$ events, followed by their full simulation in the DØ detector. The W+jets events, which correspond to the dominant background, were generated by "matched" ALPGEN as a function of jet multiplicity, separately for each quark flavor, using the "MLM" matching scheme [49]. These separated samples were then added together with appropriate event weights to provide a correct mix. Because of this feature and the need to simulate identification efficiencies, weighted simulated $t\bar{t}$ and W+jets events had

to be used in testing ensembles representing signal and background, as will be described later. Weights were used in deciding whether to include an event in the ensemble. Because of limitations in computing time, no heavy-flavor content was used in W+jets. However, a corrected fraction of $t\bar{t}$ in each tagged subsample was used to take account of $Wb\bar{b}$+jets states. The effect of the different topologies for $Wb\bar{b}$+jets and W+jets in the correction of the procedure was studied and included as a systematic uncertainty of the analysis. The multijet background, in which a jet is misinterpreted as a lepton, is estimated from data in which leptons are required to pass minimal selections, but fail tighter requirements.

5.2   Final Selection and Sample Composition

The analyzed data sample corresponds to 913 (e+jets) and 871 (μ+jets) events/pb of data. The events in the sample are required to pass the following selection criteria:

- Only four jets with $p_\mathrm{T} > 20\,\mathrm{GeV}$ and $|\eta| < 2.5$.

- An isolated electron or muon with $p_\mathrm{T} > 20\,\mathrm{GeV}$, and $|\eta| < 2$ for muons, or $|\eta| < 1.1$ for electrons.

- $\not{E}_\mathrm{T} > 20\,\mathrm{GeV}$.

The rejection of events with more than four jets is motivated by the fact that the analysis is based on a signal probability P_sgn calculated using a leading-order matrix element for $t\bar{t}$ production. In the leading-order scheme, decays that present additional radiation, as well as $t\bar{t}$ pairs produced in association with other (gluon) jets, are not considered. The exclusive four-jets requirement therefore minimizes the number of such events in the selected sample. A total of 251 e+jets and 256 μ+jets events are selected for the analysis.

Channel	N_{evts}	f_{top}	f_{Wjets}	f_{QCD}
e+jets	251	$27.6 \pm 6.2\%$	$57.3 \pm 6.8\%$	$15.1 \pm 1.3\%$
μ+jets	256	$25.4 \pm 5.3\%$	$66.2 \pm 6.0\%$	$8.36 \pm 1.1\%$

Table 5.1: Fractional compositions (f) for e+jets and μ+jets data samples before b-tagging, as estimated using the topological likelihood technique [46]. "QCD" is used as a shorthand to signify multijet background.

5.2.1 Composition Before b-tagging

The response studies of the analysis presented in next chapter require to assume a $t\bar{t}$ signal fraction. One way to determine the $t\bar{t}$ signal fraction to use in the response studies is to define a likelihood discriminant based on topological variables for each selected event, as described in Ref. [50]. A fit to the observed distribution to the discriminant yields the fractions of $t\bar{t}$, W+jets, and multijet events in the data sample, separately for e+jets and μ+jets events. The results of fits are summarized in Table 5.1, were the sample composition was determined before applying b-tagging criteria.

The likelihood discriminant determined only the fraction of signal and background events to use in the response studies, and did not affect fits to the mass of the top quark. As an alternative, we could have chosen to use the fractions extracted from the eventual fit to the mass (Matrix Element).

5.2.2 Composition After b-tagging

The number of events in each subsample, after b-tagging, is summarized in Table 5.2 for e+jets and μ+jets. Also in the Table, are the number of events predicted by the tag-rates functions (TRF) for e+jets, and are in very good agreement with what is observed in data.

channel	N_{evts}	0 b-tag	1 b-tag	2 b-tag
e+jets	251	173	57	19
μ+jets	256	163	70	22
TRF(e+jets)	251	186(7)	46(6)	19(4)

Table 5.2: Composition of the e+jets and μ+jets for b-tagged data samples using, the "Medium" operating point in the NN tagger. Also shown for comparison are the TRF predictions used in the response studies for the e+jets sample, with the uncertainties given in brackets.

Chapter 6

Measurement of the Mass of the Top Quark Using the Matrix Element Method

The measurement of the mass of the top quark using the Matrix Element method (ME) is described in this chapter. Our ME method is similar to the one developed in Ref [51], except that we allow a simultaneous measurement of the mass of the top quark m_{top} and of the jet energy scale JES, as suggested in Ref. [53].

An overview of the Matrix Element method is given in Section 6.1. The likelihood fit to the mass m_{top} is described in Section 6.2. The study of the response of the method in a simplified case is shown in Section 6.3. Section 6.4 discusses the corrections to the response for analyzing the data.

6.1 The Matrix Element (ME) Method

To ME method maximizes the use of the statistical information extracted from the event sample calculating by a probability for each event to represent a spesified process. These probabilities are calculated as a function of the assumed top-quark mass (m_{top}) and jet energy scale (JES), and depend on all the measured quantities in an event The probabilities from all events in the sample are then combined to obtain the sample probability as a function of assumed mass and jet energy scale, and the top-quark mass and JES are extracted by finding the values that maximize this probability.

The probability P_{evt} for any event is composed from probabilities for two processes, $t\bar{t}$ and W+jets production:

$$P_{evt}\left(x;\, m_{\text{top}},\, JES,\, f_{\text{top}}\right) = f_{\text{top}} \cdot P_{\text{sgn}}\left(x;\, m_{\text{top}},\, JES\right) + \left(1 - f_{\text{top}}\right) \cdot P_{\text{bkg}}\left(x\right) \ . \quad (6.1)$$

where x represents the kinematic variables of the event (jet and lepton energies and angles), f_{top} is the signal fraction in the event sample, and P_{sgn} and P_{bkg} are the probabilities for $t\bar{t}$ and W+jets production, respectively.

Multijet production (or "QCD") is the second most important background, however, its character is similar to that of W+jets, and is not included separately in the background calculation. The effect of the difference in dependence on x for QCD and W+jets is accounted for in the systematic uncertainty of the analysis. Other background contributions are negligible.

As indicated above, for each measured event, the signal probability P_{sgn} is calculated as a function of two parameters: the top mass m_{top} and the jet energy scale JES. The background probability P_{bkg} does not depend on m_{top}, and the jet energy scale is kept constant at $JES = 1$, as argued below.

The reason to fix the JES in $P_{\rm bkg}$ is that the JES parameter is used to adjust for a possible overall miscalibration of the jet energy scale. Because the W mass is fixed in the matrix element for signal, the likelihood for $t\bar{t}$ signal as a function of JES will be maximal when the invariant mass of the two light jets gives the correct W mass. The JES parameter will therefore compensate for small overall miscalibrations in the energy of jets by taking advantage of the mass constraint on the W. For background events, there is no such constraint since there is either a leptonically decaying W boson (as in W+jets events) or no W at all (as in QCD events), thus the W mass constraint exists only for $t\bar{t}$ signal events. Unfortunately, an event by event signal to background distinction cannot be made, and it is therefore best to let events with a large $P_{\rm sgn}/P_{\rm bkg}$ ratio affect the likelihood when JES is varied, while making sure there is little or no impact on the likelihood for events with a small $P_{\rm sgn}/P_{\rm bkg}$ ratio. As is the case for the $m_{\rm top}$ parameter, background-like events should not be allowed to contribute in the setting of JES, and hence is fixed to 1 in the calculation of the background probability.

6.1.1 Signal Probability

When every quantity in a collision is available at the parton level, the probability P that an event corresponds to some specific production process can be obtained from the differential cross section for that process:

$$P(y) = d\sigma(y)/\sigma(y) \tag{6.2}$$

with

$$d\sigma(y) = |\mathscr{M}(y)|^2 \Phi(y) dy \tag{6.3}$$

where y corresponds to the parton-level quantities that define these events, $\Phi(y)$ is the phase space for the specific transition, $\mathscr{M}(y)$ is the amplitude for the process under study, and $\sigma(y)$ is the total cross section for the process.

For these ideal circumstances, it is straightforward to write a probability for the event to correspond to signal or to some background process. And this $P(y)$ would be the best possible discriminator, since it would include all the information that characterizes the event. In our experiment, however, we do not have such parton-level information.

We can measure the directions of jets and lepton (10 angles) with good precision, and regard them as equivalent to those of the originally produced objects. With the constraint of energy and momentum conservation in the collision, we therefore have a total of 14 constraints. A total of 23 quantities are used to define a complete $p\bar{p} \rightarrow t\bar{t} \rightarrow \ell+4$ jets event: 18 for the 6 final-state particles (including the neutrino), 2 for the initial partons (ignoring any transverse "Fermi" motion), and 3 for the vector momentum to allow to account for small but finite initial state radiation (ISR). We must therefore integrate over 9 variables to define the probability of an event corresponding to $t\bar{t}$ production at some fixed m_{top} and JES values.

There is freedom in choosing the variables to integrate over, and these are chosen to maximize calculational efficiency. For example, for true $t\bar{t}$ events, the system composed of the electron and neutrino correspond to the W, and when combined with one of the b-quarks, they reconstruct the original top quark. We can therefore choose the invariant mass of the $e\nu$ system, instead of using the longitudinal momentum of the neutrino as an integration variable. Also, using the invariant mass of the $e\nu b-$jet system instead of the energy of the $b-$jet as an integration variable is more efficient. Similarly, in the hadronic branch of the W, we can choose the invariant mass of the two light jets and the invariant mass

of these combined with the remaining b-quark jet as two other variables. The energy of one of the light jets (ρ_1) is used as the fifth variable of integration. The above procedure is not appropiate for background, since the two light jets do not correspond to decay products of a single W particle. For the W+jets background, the energies of the 4 jets are more efficient variables, along with the invariant mass of the $e\nu$ system. The remaining variables are the energy of the lepton integrated over its resolution, and the vector momentum of the $t\bar{t}$ system, representing any emitted ISR.

The choice of variables defines a Jacobian for the transformation of variables. The same procedure adopted in Ref. [51] is used here, but with a slightly revised version of the Jacobian.

The differential probability to observe a $t\bar{t}$ event with kinematic values x in the detector is then given by:

$$
\begin{aligned}
P_{\text{sgn}}(x;\, m_{\text{top}}, JES) \;=\;\; & \frac{1}{\sigma_{\text{obs}}(p\bar{p} \to t\bar{t};\, m_{\text{top}}, JES)} \\[2mm]
& \sum_{perm} w_i \int_{q_1, q_2, y} \sum_{flavors} \mathrm{d}q_1 \mathrm{d}q_2 f(q_1) f(q_2) \\[2mm]
& \frac{(2\pi)^4 \left| \mathscr{M}(q\bar{q} \to t\bar{t} \to y) \right|^2}{2 q_1 q_2 s} \mathrm{d}\Phi_6 W(x, y;\, JES)
\end{aligned}
$$

(6.4)

Where s is the square of the $p\bar{p}$ center-of-mass energy, q_1 and q_2 are the momentum fractions of the colliding partons (assumed to be massless) within the colliding proton and antiproton, $f(q)$ denotes the probability density for finding a parton of given flavor and momentum fraction q in a proton or antiproton.

The finite resolution of the detector is taken into account via a convolution with a transfer function $W(x, y;\, JES)$ that gives the probability for reconstructing a

partonic final state y given the objects characterized by x in the detector. The differential element $d\Phi_6$ of the six-body phase space as a function of the variables $(\overrightarrow{\Omega}_{jets}, \rho_1, m_{d\bar{u}}, m_{\bar{b}d\bar{u}}, m_{\bar{e}\nu}, m_{b\bar{e}\nu}, \overrightarrow{p}_e)$ is given by [52]:

$$
\begin{aligned}
d\Phi_6 &= [\delta(E_{q_1} + E_{q_2} - \sum_{i=1}^{6} E_i)][\delta(p_{q_1}^z + p_{q_2}^z - \sum_{i=1}^{6} p_i^z)] \; \frac{d^3\overrightarrow{p}_e}{(2\pi)^3 2E_e} \frac{d\rho_1}{(2\pi)^3 2E_\nu} \\
&\quad \times \prod_{i=1}^{4} \frac{\rho_i^2 d\Omega_i}{(2\pi)^3 2E_i} \frac{dm_{d\bar{u}}^2 dm_{\bar{b}d\bar{u}}^2}{|JA|} \frac{dm_{\bar{e}\nu}^2 dm_{b\bar{e}\nu}^2}{|JL|} \\
&= \frac{4}{(2\pi)^4} \Phi_6 \, [\delta(E_{q_1} + E_{q_2} - \sum_{i=1}^{6} E_i)] \, [\delta(p_{q_1}^z + p_{q_2}^z - \sum_{i=1}^{6} p_i^z)] \\
&\quad \times d^3\overrightarrow{p}_e \, d\rho_1 dm_{d\bar{u}}^2 dm_{\bar{b}d\bar{u}}^2 dm_{\bar{e}\nu}^2 dm_{b\bar{e}\nu}^2 \prod_{i=1}^{4} d\Omega_i
\end{aligned}
\tag{6.5}
$$

with

$$
\Phi_6 = \frac{4}{(4\pi)^{14}} \frac{1}{E_e E_\nu} \prod_{i=1}^{4} \frac{\rho_i^2}{E_i} \frac{1}{|JA||JL|}
\tag{6.6}
$$

$$
\tag{6.7}
$$

and

$$
\begin{aligned}
|JA| &= |2E_1 \frac{\rho_2}{E_2} - 2\rho_1 cos\theta_{12}||2E_1 \frac{\rho_3}{E_3} - 2\rho_1 cos\theta_{13} + 2E_2 \frac{\rho_3}{E_3} - 2\rho_2 cos\theta_{23}| \\
|JL| &= |2E_e \frac{p_\nu^z}{E_\nu} - 2p_e^z||2E_e \frac{\rho_4}{E_4} - 2\rho_e cos\theta_{e4} + 2E_\nu \frac{\rho_4}{E_4} - 2\rho_\nu cos\theta_{\nu4}| \\
&\quad - sin\theta_4 sin\phi_4(a_y b_z - a_z b_y) - sin\theta_4 cos\theta_4(a_x b_z - a_z b_x)
\end{aligned}
\tag{6.8}
$$

with

$$
\begin{aligned}
a_i &= (E_e + E_4)\frac{\rho_\nu^i}{E_\nu} - \rho_e^i - \rho_4^i \\
b_i &= (E_e)\frac{\rho_\nu^i}{E_\nu} - \rho_e^i
\end{aligned}
\tag{6.9}
$$

where E_i are the energies of the final state objects, $\rho_i = |\vec{p}^{\,i}_{jet}|$, $m_{d\bar{u}}$ is the invariant mass of the $d\bar{u}$ system and $m_{\bar{b}d\bar{u}}$ is the invariant mass of the $\bar{b}d\bar{u}$ system, $m_{\bar{e}\nu}$ is the invariant mass of the $\bar{e}\nu$ system and $m_{b\bar{e}\nu}$ is the invariant mass of the $b\bar{e}\nu$ system.

Because it is not known which parton evolves into which jet, a sum must be carried out over all 24 permutations of jet-to-parton assignments. The variable w_i represents the weight attributed to each permutation and is described next.

The symbol $\mathcal{M}$ denotes the matrix element for the process $q\bar{q} \rightarrow t\bar{t} \rightarrow b(\bar{\ell}\nu)^+\bar{b}(q\bar{q}')^-$ averaged over initial quark color and spins, and summed over the final colors and spins:

$$
\begin{aligned}
|\mathcal{M}|^2 &= \frac{g_s^4}{9}F\overline{F}\Bigg((2 - \beta^2 s_{qt}^2) \\
&\quad - \frac{(1 - c_{\bar{e}q}c_{d\bar{q}}) - \beta(c_{\bar{e}t} + c_{d\bar{t}}) + \beta c_{qt}(c_{\bar{e}q} + c_{d\bar{q}}) + \frac{1}{2}\beta^2 s_{qt}^2(1 - c_{\bar{e}d})}{\gamma^2(1 - \beta c_{\bar{e}t})(1 - \beta c_{d\bar{t}})}\Bigg)
\end{aligned}
\tag{6.10}
$$

where s_{ij} and c_{ij} are the sine and cosine of the angle between particles i and j, calculated in the $q\bar{q}$ center of mass (CM), g_s is the strong coupling constant ($g_s^2/4\pi = \alpha_s$), β is the top quark's velocity (relative to the speed of light) in the $q\bar{q}$ CM, and $\gamma = (1 - \beta^2)^{-1/2}$. The second term in $\mathcal{M}$ reflects $t\bar{t}$ spin correlations and, as was done in the previous analysis, was not considered in the extraction of m_{top}.

F represents to the leptonic-decay kinematics of the top quark ($t \to W^+ b \to \overline{e}\nu_e b$):

$$F = \frac{g_w^4}{4} \left[\frac{m_{b\overline{e}\nu}^2 - m_{\overline{e}\nu}^2}{(m_{b\overline{e}\nu}^2 - m_{\text{top}}^2)^2 + (m_{\text{top}}\Gamma_t)^2} \right] \left[\frac{m_{b\overline{e}\nu}^2(1 - \hat{c}_{\overline{e}b}^2) + m_{\overline{e}\nu}^2(1 + \hat{c}_{\overline{e}b})^2}{(m_{\overline{e}\nu}^2 - m_W^2)^2 + (m_W\Gamma_W)^2} \right] \quad (6.11)$$

where $\hat{c}_{\overline{e}b}$ is the cosine of the angle between $\overline{e}$ and b in the W^+ rest frame, $(m_{\text{top}}, \Gamma_t)$ and (m_W, Γ_W) are the masses and widths of the top quark and W boson, and g_w is the weak coupling constant ($G_F/\sqrt{2} = g_w^2/8m_W^2$). Similarly, $\overline{F}$ corresponds to the decay $\overline{t} \to W^- \overline{b} \to d\overline{u}\overline{b}$:

$$\overline{F} = \frac{g_w^4}{4} \left[\frac{m_{\overline{b}d\overline{u}}^2 - m_{d\overline{u}}^2}{(m_{\overline{b}d\overline{u}}^2 - m_{\text{top}}^2)^2 + (m_{\text{top}}\Gamma_t)^2} \right] \left[\frac{m_{\overline{b}d\overline{u}}^2(1 - \hat{c}_{d\overline{b}}^2) + m_{d\overline{u}}^2(1 + \hat{c}_{d\overline{b}})^2}{(m_{d\overline{u}}^2 - m_W^2)^2 + (m_W\Gamma_W)^2} \right] \quad (6.12)$$

where $\hat{c}_{d\overline{b}}$ is the cosine of the angle between d and $\overline{b}$ in the W^- rest frame, m_{top} is the parameter that maximizes the likelihood and corresponds to the extracted mass. The W bosson mass is fixed to the known value $m_W = 80.4$ GeV [7] and is used to adjust the JES.

Signal Probability When Using b-tagging

When we ignore b-tagging information (untagged), we have $w_i = 1/24$, since no extra information is used to determine which permutation is more likely to be right. When using b-tagging information, w_i is defined by the normalized product of the probabilities p_j of tagging each jet j:

$$w_i = \frac{1}{\Sigma_{i=1,24}\; w_i} \Pi_{j=1,4}\; p_j \quad (6.13)$$

The probabilities for a jet to be tagged, $\epsilon_j(\alpha_j; E_{t,j}, \eta_j)$, are given by the Tag Rate Functions (TRF), which are parameterizations of b-tagging efficiencies as a

function of the jet's transverse energy E_T and pseudorapidity η, and the flavor α of the originating parton.

That is,

$$p_j = \epsilon_j(\alpha_j; E_{t,j}, \eta_j) \tag{6.14}$$

when a jet is tagged and

$$p_j = 1 - \epsilon_j(\alpha_j; E_{t,j}, \eta_j) \tag{6.15}$$

when the jet is not tagged. The TRF are also defined for each NN operating point, and, as indicated previously, "Medium" is used in our analysis.

Because the tagging efficiencies for c quarks cannot be neglected, both $u\bar{d}$ and $c\bar{s}$ decay modes for the hadronic W are considered in our analysis:.

$$P_{\text{sgn}} = \frac{1}{2}\left(P_{\text{sgn}}^{W\to u\bar{d}} + P_{\text{sgn}}^{W\to c\bar{s}}\right) \tag{6.16}$$

Normalizing the Probability

The overall detector efficiency (f_{acc}) depends both on m_{top} and on the jet energy scale. This is taken into account in the cross section for $t\bar{t}$ events observed in the detector:

$$
\begin{aligned}
\sigma_{\text{obs}}(p\bar{p} \to t\bar{t}; m_{\text{top}}, JES) &= \int\limits_{q_1,q_2,x,y} d\sigma(p\bar{p} \to t\bar{t} \to y; m_{\text{top}})W(x,y; JES)f_{\text{acc}}(x) \\
&= \left\{\int\limits_{q_1,q_2,x,y} d\sigma(p\bar{p} \to t\bar{t} \to y; m_{\text{top}})\right\} \\
&\quad \times \frac{1}{M}\sum_{acc}(\text{event weight}) \ .
\end{aligned}
\tag{6.17}
$$

where M is the number of generated Monte Carlo events, and the sum runs over all events that pass the selections, event reconstruction efficiency, etc. Because of trigger restrictions and different ID efficiencies, different Monte Carlo events can carry different weights. The sum in Eq. 6.17 therefore requires summing these weights for all events that are accepted. The dependence of the total $t\bar{t}$ cross section on m_{top} for $q\bar{q} \rightarrow t\bar{t}$ at $\sqrt{s} = 1.96$ GeV from Eq. 6.17 is given in Fig. 6.1. The dependence of the acceptance on m_{top} and JES for e+jets and μ+jets MC samples is given in Fig. 6.2.

Reducing Assumptions - Considering ISR and Electron Resolutions

In previous implementations of the ME analysis, it was assumed that the transverse momentum p_T of the $t\bar{t}$ system could be neglected in ℓ+4 jets $t\bar{t}$ events. Also the energy resolution for electrons was considered negligible. These two assumptions were dropped in this analysis, and thereby yielded an improved measurement of m_{top}.

To include a finite p_T of the $t\bar{t}$ system to account for ISR, and to consider electron energy resolution, leads to a more realistic description of the probability, but it also requires additional computing time which limited previous analyses. This was resolved through the development of an optimized MC integration, and acquiring more computing power at DØ. The inclusion of energy resolution for electrons as well as the other issues in detector response are considered in Section 6.1.3 below.

To account for ISR, the expected p_T spectrum for the produced $t\bar{t}$ system was extracted directly from PYTHIA and used in this analysis as a probability distribution function in the MC integration for the signal probability in Eq. 6.4 and its normalization. The inclusion of these two additional aspects provided a
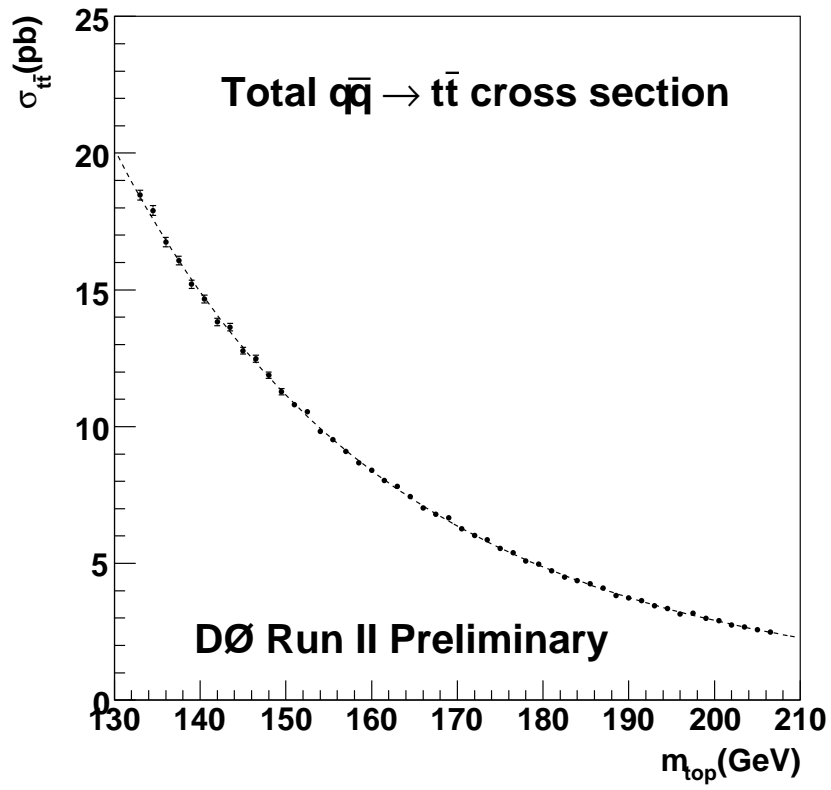
Figure 6.1: The calculated total $t\bar{t}$ production cross section at $\sqrt{s} = 1.96$ GeV [48] as a function of the top mass, used in the normalization of the signal probability (gg contribution is ignored).
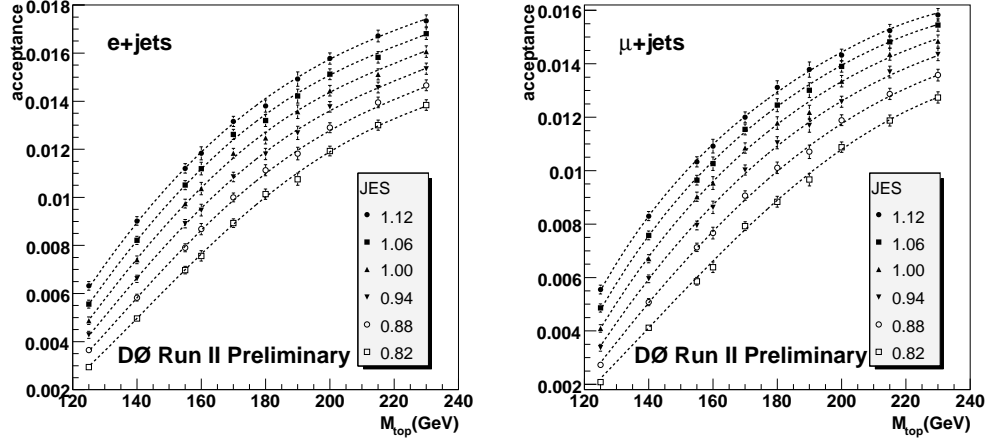
Figure 6.2: The dependence of the overall acceptance on the top mass and JES for e+jets (left) and μ+jets (right) MC $t\bar{t}$ samples.

more consistent description of the parameters and uncertainties in the analysis, and, as mentioned above, provided an improved measurement of m_{top}. For clarity, we summarize the main assumptions in the calculation of signal probability used in previous work [51]:

- Jets and lepton angles are measured perfectly well in the detector.

- Energy resolution of jets and leptons, are independent, and can be factorized as the product of individual resolution functions.

- Contribution from $gg \to t\bar{t}$ is small at the Tevatron, and is not included in the probability calculation.

- Spin correlations in the ME do not have much impact on the extracted value of m_{top}.

- We ignore final state radiation (FSR) in ℓ+4 jets events.

(Similar assumptions are made in the calculation of the background probability, as described below.)

Although several of the above assumptions may seem ad hoc, the effects are examined and corrected in calibration studies using MC event ensembles, using realistic simulations of the data. After such calibration, any differences observed between data and MC are folded into the systematic uncertainties of the analysis.

6.1.2 Background Probability

The expression for the background probability P_{bkg} is similar to that for P_{sgn} in Eq. 6.4, except that the VECBOS [54] parameterization of the matrix element $\mathscr{M}$ for W production is used, and all jets are assumed to be light. Since the matrix element for W+jets production does not depend on m_{top}, P_{bkg} is independent of m_{top}. Also, as discused above, the choice of integration variables in the calculation changes to use the energy of the 4 different jets and the invariant mass of the electron-neutrino system.

Another important difference, as mentioned before, is the choice of making the background probability independent of the JES variable. This choice assures that the measurement of JES is not determined by events with a high probability of being background. That is, the contribution to the dependence of the likelihood on JES is based on well reconstructed $t\bar{t}$ events of large P_{sgn}/P_{bkg} ratio.

Below we summarize the main assumptions used in the calculation of the background probability:

- Jets and lepton angles are measured perfectly well.

- Resolutions for jets and lepton energies can be factorized as the product of individual resolution functions.

- All jets in the event are assumed to have light flavor.

- There is no final-state radiation.

And, as in the case of $t\bar{t}$ signal, the effects of these assumptions are examined and corrected using realistic fully simulated events used in the calibration of the method, and any differences between data and MC are considered in the systematic uncertainties of the analysis.

6.1.3 Description of Detector Response

The resolutions for the measurement of jets and leptons in the events are represented by the transfer function $W(x, y; JES)$, which factorizes into contributions from the individual $t\bar{t}$ decay products. The approximation is that the resolution for different objects are not correlated. Because the angles of all observed $t\bar{t}$ decay products are assumed to be well measured (described by δ-functions), this reduces the dimensions of the integration in Eq. 6.4 over 6-particle phase space. In this section, we discuss the integrations over the jet and electron energies and over the transverse momentum of muons, taking account of the respective resolutions.

Parameterization of the Jet Energy Resolution

The transfer functions for calorimeter jets are directly related to the resolution in the mass measurement of the analysis. This transfer function $W_{\mathrm{jet}}(E_x, E_y; JES)$ yields the probability for measuring E_x in the detector if the true quark energy is E_y.

For the case $JES = 1$, it is parameterized as:

$$
\begin{aligned}
W_{\text{jet}}(E_x, E_y) \;=\; & \frac{1}{\sqrt{2\pi}(p_2 + p_3 p_5)} \\
& \left[\exp\left(-\frac{((E_x - E_y) - p_1)^2}{2p_2^2} \right) + p_3 \exp\left(-\frac{((E_x - E_y) - p_4)^2}{2p_5^2} \right) \right]
\end{aligned}
\tag{6.18}
$$

where the p_i are parameterized further as linear functions of quark energy:

$$
p_i = a_i + E_y \cdot b_i \tag{6.19}
$$

with a_3 set to 0.

The parameters a_i and b_i are determined from simulated $t\bar{t}$ events for a range of m_{top}, after applying all standard DØ jet energy corrections. The parton and reconstructed jet energies in events are used to minimize an unbinned likelihood fit to W_{jet} with respect to the a_i and b_i parameters. A different set of parameters is derived for each of four η regions: $|\eta| < 0.5$, $0.5 < |\eta| < 1.0$, $1.0 < |\eta| < 1.5$, and $1.5 < |\eta| < 2.5$, and for three varieties of quarks: light quarks (u, d, s, c), b quarks with a soft muon tag in the associated jet, and all other b quarks.

For $JES \neq 1$, the jet transfer function is adapted as follows:

$$
W_{\text{jet}}(E_x, E_y; JES) = \frac{W_{\text{jet}}(\frac{E_x}{JES}, E_y, 1)}{JES} \tag{6.20}
$$

The JES factor is needed in the denominator to preserve the normalization:

$$
\int W_{jet}(E_x, E_y; JES)\, \mathrm{d}E_x = 1 \tag{6.21}
$$

An example of Monte Carlo derived transfer functions for light jets is shown in
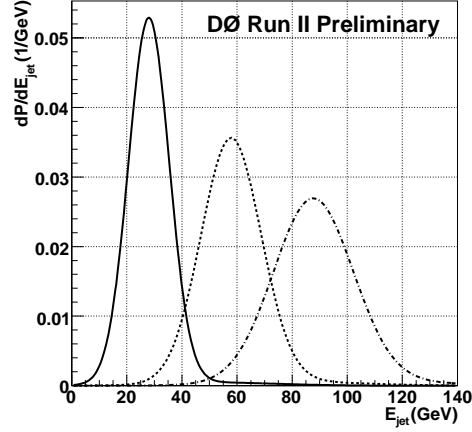
Figure 6.3: Transfer functions for light quark jets for parton energies of 30 (solid), 60 (dashed) and 90 (dashed-dotted) GeV in the central region of $|\eta| < 0.5$, for the reference jet energy scale JES=1.

Fig 6.3 for energies of 30, 60 and 90 GeV and JES=1 and $|\eta| < 0.5$.

Parameterization of the Momentum Resolution of the Muon

The transfer function W_μ, describes the resolution of the central tracking chamber in reconstructing tranverse momenta of muons. The resolution of the quantity given by the electric charge divided by the transverse momentum of a particle is considered as a function of pseudorapidity and is parameterized as:

$$W_\mu \left((q/p_T)_{\mu,\,x} , (q/p_T)_{\mu,\,y} \right) = \frac{1}{\sqrt{2\pi}\sigma} \exp\left(-\frac{1}{2} \left(\frac{(q/p_T)_{\mu,\,x} - (q/p_T)_{\mu,\,y}}{\sigma} \right)^2 \right)$$

$$(6.22)$$

where q denotes the charge and p_T the transverse momentum of a generated (y) muon or its reconstructed track (x). The resolution:

$$\sigma = \begin{cases} \sigma_0 & \text{for } |\eta| \leq \eta_0 \\ \sqrt{\sigma_0^2 + [c\,(|\eta| - \eta_0)]^2} & \text{for } |\eta| > \eta_0 \end{cases} \qquad (6.23)$$

is obtained from muon tracks in MC events, where the above parameters are taken as linear function of $1/p_T$:

$$\begin{aligned} \sigma_0 &= \sigma_0(0) + \sigma_0(1) \cdot 1/p_T \\ c_0 &= c_0(0) + c_0(1) \cdot 1/p_T \\ \eta_0 &= \eta_0(0) + \eta_0(1) \cdot 1/p_T \end{aligned} \qquad (6.24)$$

The values of the coefficients are given in Table 6.1 for "pre-shutdown" and "post-shutdown" data taking periods (which divide the full data sample approximately in two), as a function of whether the μ tracks are associated with hits in the silicon tracker.

The muon charge is not used in the calculation of P_{sgn} and P_{bkg}. However, for muons with large transverse momentum, it is important to consider the possibility of charge misidentification in the transfer function.

Parameterization of the Energy Resolution of Electrons

In previous implementations of the ME analysis, the electron resolution was assumed to be perfect (a δ-function). In the present analysis, electron energy resolution is considered finite and comes into the integration over its energy.

The electron energy resolution is parameterized by the following transfer func-

parameter	with silicon hits		no silicon hits	
	pre	*post*	*pre*	*post*
$\sigma_0(0)$	1.800×10^{-3}	2.066×10^{-3}	2.665×10^{-3}	2.968×10^{-3}
$\sigma_0(1)$	1.604×10^{-2}	2.219×10^{-2}	1.392×10^{-2}	2.913×10^{-2}
$c_0(0)$	4.958×10^{-3}	5.557×10^{-3}	1.456×10^{-2}	1.649×10^{-2}
$c_0(1)$	9.085×10^{-2}	1.190×10^{-1}	5.826×10^{-2}	-3.035×10^{-2}
$\eta_0(0)$	1.4	1.4	1.4	1.4
$\eta_0(1)$	0.	0.	0.	0.

Table 6.1: Muon transfer-function parameters for pre-shutdown and post-shutdown data-taking periods, as a function of whether silicon hits are associated with the μ tracks found in the outer muon tracker.

tion:

$$W_e\left(E_x, E_y\right) = \frac{1}{\sqrt{2\pi}\sigma} \exp\left[-\frac{1}{2}\left(\frac{E_x - E_y}{\sigma}\right)^2\right] \qquad (6.25)$$

where:

$$E_x = \text{reconstructed electron energy}$$

$$E_y = 1.0002 \cdot E_{\text{true}} + 0.324$$

$$\sigma = \sqrt{(0.028 \cdot E_y)^2 + (S \cdot E_y)^2 + (0.4)^2}$$

$$S = \frac{0.164}{\sqrt{E_y}} + \frac{0.122}{E_y} \exp\left(\frac{p_1}{\sin\{2\arctan[\exp(-\eta_e)]\}}\right) - p_1$$

$$p_1 = 1.35193 - \frac{2.09564}{E_y} - \frac{6.98578}{E_y^2}.$$

This parameterization was formulated by the DØ W-mass Group[55].

6.2   The Multidimensional Likelihood

A likelihood function is constructed from individual event probabilities for a set of n measured events $x_1, .., x_n$, and calculated according to Eq. 6.1 as:

$$L(x_1, .., x_n; m_{\text{top}}, JES, f_{\text{top}}) = \prod_{i=1}^{n} P_{\text{evt}}(x_i; m_{\text{top}}, JES, f_{\text{top}}) \qquad (6.26)$$

For every assumed pair of values of (m_{top}, JES), the value of likelihood L is maximized as a function of f_{top}, yielding $f_{\text{top}}^{\text{best}}$. The mass of the top quark and jet energy scale are then extracted by projecting:

$$L(x_1, .., x_n; m_{\text{top}}, JES) = L\left(x_1, .., x_n; m_{\text{top}}, JES, f_{\text{top}}^{\text{best}}(m_{\text{top}}, JES)\right) \qquad (6.27)$$

onto the m_{top} axis:

$$L(x_1, .., x_n; m_{\text{top}}) = \int L(x_1, .., x_n; m_{\text{top}}, JES)\, \mathrm{d}(JES) \qquad (6.28)$$

and similarly for the JES variable,

$$L(x_1, .., x_n; JES) = \int L(x_1, .., x_n; m_{\text{top}}, JES)\, \mathrm{d}(m_{\text{top}}) \qquad (6.29)$$

The mean (or peak) and the RMS (or half width) of $L(x_1, .., x_n; m_{\text{top}})$ and $L(x_1, .., x_n; JES)$ are then used to extract the best estimate of the top mass, the JES and their uncertainties. The projections given by Eq. 6.28 and Eq. 6.29 assume no prior knowledge of jet energy scale.

6.2.1 Adding Prior Knowledge of JES to the Measurement

Although the above in-situ calibration of JES provides an improvement compared to adding the JES as a systematic uncertainty, we can go further using an independent measure of the JES to constrain our likelihood. The improvement depends only on the resolution of the external measurement compared to that of the in-situ calibration. The limits to improvement range from: (i) the ideal case, when JES is known perfectly, and yields a one dimensional (1D) likelihood as function of m_{top}, and (ii) the limit where the external measurement is so poor (equivalent to a flat JES prior) that it does not constrain the in-situ calibration at all, which, in fact, increases the statistical uncertainty on m_{top} by 50%.

If there is prior information of the JES, then instead of projecting as in Eq. 6.28, we use[56]:

$$L\left(x_1, .., x_n; m_{\text{top}}\right) = \int L\left(x_1, .., x_n; m_{\text{top}}, JES\right) G\left(JES\right) \text{d}\left(JES\right) \qquad (6.30)$$

Where, in our particular case, we choose the prior $G\left(JES\right)$ to be a Gaussian function, centered at $JES = 1$ with an RMS width of $\sigma = 0.037$. The RMS width is calculated using the uncertainty on the jet energy scale derived from a γ+jets sample of data by the DØ Jet Energy Scale Group (JESG). The distribution in fractional uncertainties of JES based on the results from JESG for jets from a $t\bar{t}$ Monte Carlo sample are shown in Fig. 6.4. The mean fractional uncertainty in this figure is used as the RMS on the JES prior.

6.2.2 Combining Different b-tagged Samples

When using b-tagging information, the full $t\bar{t}$ sample is divided into three categories: no tagged jets, 1 tagged jet and 2 or more tagged jets.
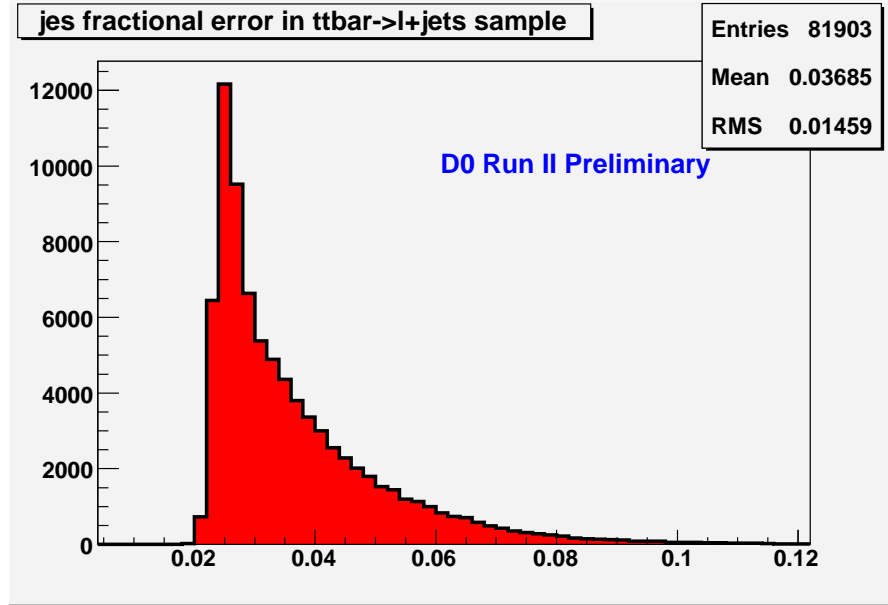
Figure 6.4: Distribution in fractional uncertainty in JES for $t\bar{t}$ Monte Carlo events generated at m_{top} =175 GeV. The average of this distribution is used as the RMS on the prior for JES.

The likelihood of Eq. 6.27 is evaluated separately for each category, with the maximization for f_{top} performed independently for each group. Subsequently, the likelihoods for the three groups are multiplied and projected onto the m_{top} axis according to Eq. 6.28 or Eq. 6.30, depending on whether a prior on JES is used in the analysis.

6.3   Response of the Method for a Simplified Case

The response of the method is first studied using fully simulated PYTHIA $t\bar{t}$ signal events described in Chapter 5, in which all four jets in each event are required to be matched to partons.

The ensembles used in these studies consist of 100 $t\bar{t}$ signal events for e+jets and for μ+jets. These events are drawn from a pool of over 2000 PYTHIA events in each of the 5 signal samples that are generated at top masses of 155, 165,170, 175 and 185 GeV. In addition, samples with $m_{\text{top}} = 170$ GeV, with all jet energies scaled by 0.95 and 1.05 are prepared in order to validate the result of using JES as a parameter. In the fit, the most likely values of m_{top} and JES are obtained for each ensemble by projecting the 2-dimensional likelihood of the ME method onto the m_{top} and JES axis respectively (see Eq. 6.28). The results of these tests are shown in Fig. 6.5 for a fixed JES $= 1$ i.e., a prior of $\delta\,(\text{JES} - 1)$, and in Fig 6.6, Fig. 6.7 and Fig. 6.8 for an unconstrained JES (i.e., a flat prior in JES). In Fig. 6.5, Fig. 6.6 , Fig. 6.7 and Fig. 6.8 we ignore b-tagging entirely. The "pulls" are given by normalized dispersions between input and fitted values of the parameters, and should equal 1.0 for Gaussian errors.
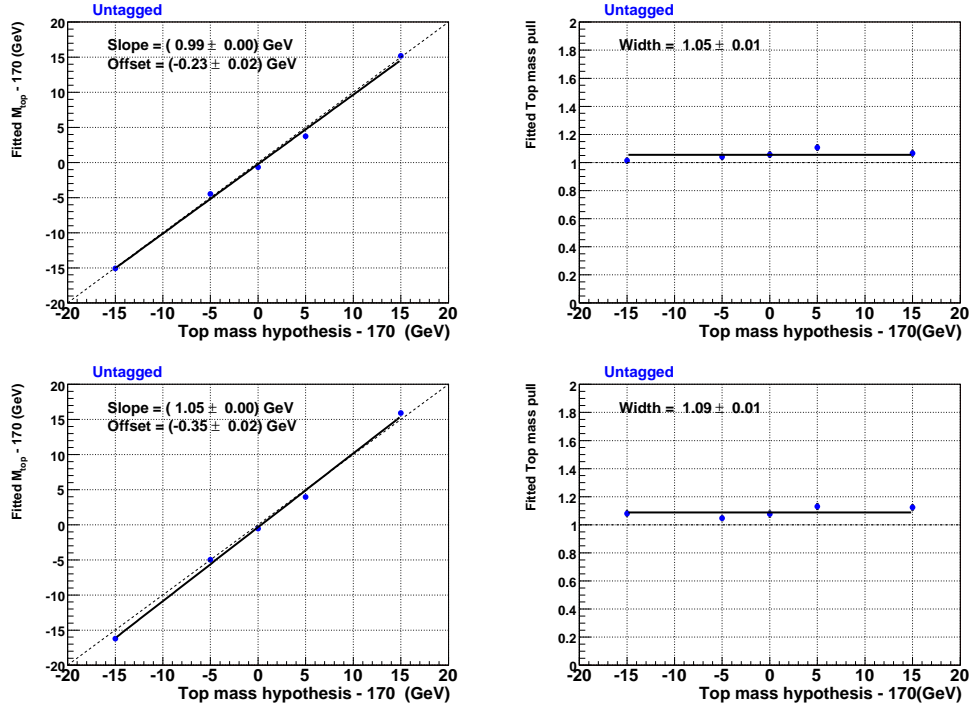
Figure 6.5: Fitted m_{top} and pulls as a function of the input top-quark mass for μ+jets (top) and e+jets (bottom), used to check or "validate" the Matrix Element method for jets matched to partons in lepton+jets $t\bar{t}$ MC events, for a JES=1 The studies ignore b-tagging information ("untagged analysis"). The dotted line represents perfect response, and the continuous line is a fit to the results of the ME analysis.
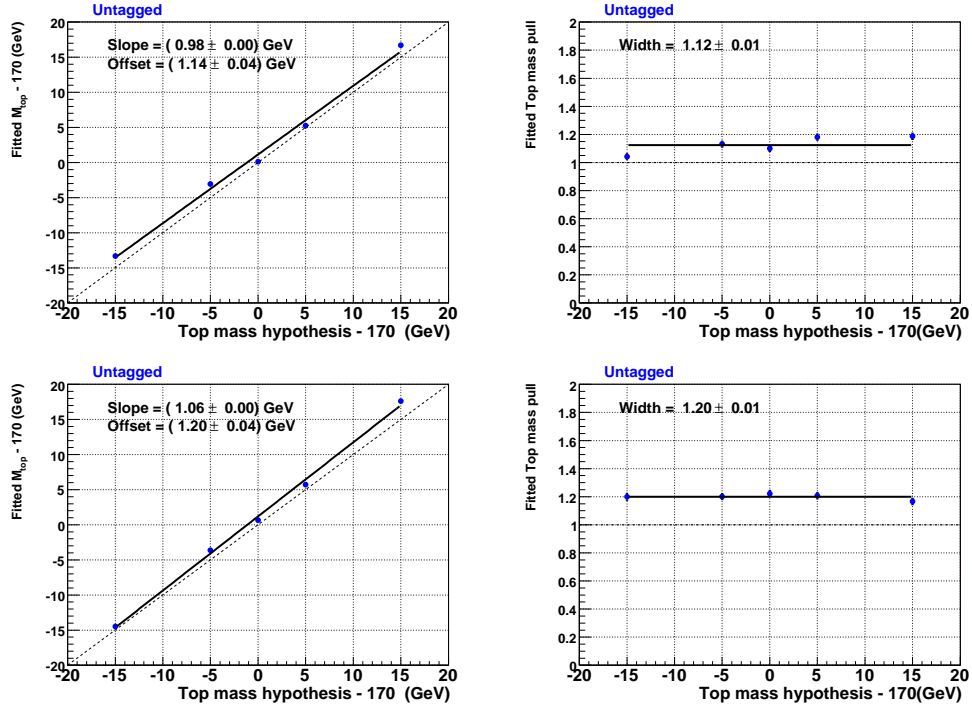
Figure 6.6: Fitted m_{top} and pulls as a function of the input top-quark mass for μ+jets (top) and e+jets (bottom), used to check or "validate" the Matrix Element method for jets matched to partons in lepton+jets $t\bar{t}$ MC events, for an unconstrained JES. The studies ignore b-tagging information ("untagged analysis"). The dotted line represents perfect response, and the continuous line is a fit to the results of the ME analysis.
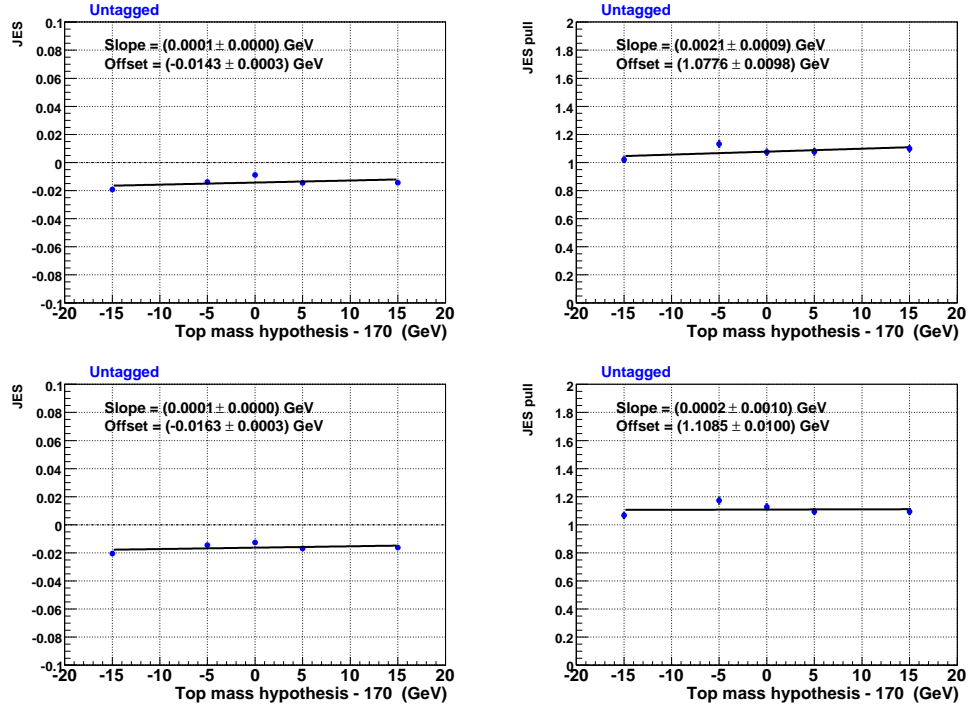
Figure 6.7: Fitted JES, and pulls as a function of the input top-quark mass for μ+jets (top) and e+jets (bottom), used to check or "validate" the Matrix Element method for jets matched to partons in lepton+jets $t\bar{t}$ MC events, for an unconstrained JES. The studies ignore b-tagging information ("untagged analysis"). The dotted line represents perfect response, and the continuous line is a fit to the results of the ME analysis.
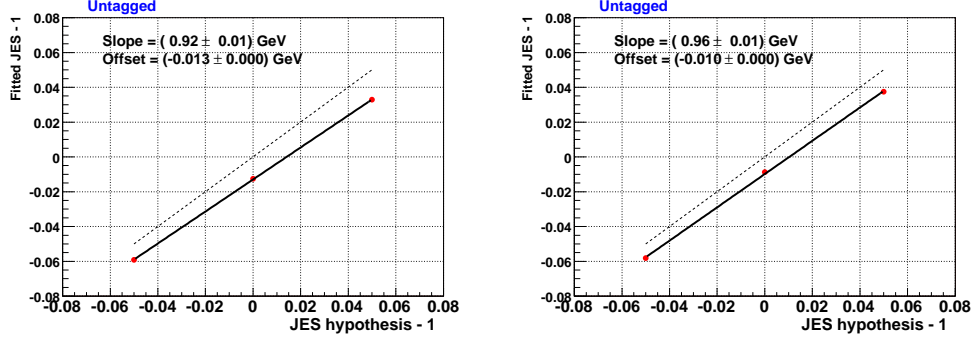
Figure 6.8: Fitted JES as function of the input JES for e+jets (left) and μ+jets (right), used to check or "validate" the Matrix Element method for jets matched to partons in lepton+jets $t\bar{t}$ MC events, for an unconstrained JES. The studies ignore b-tagging information ("untagged analysis"). The dotted line represents perfect response, and the continuous line is a fit to the results of the ME analysis.

6.4 Response of the Method for a Realistic Case

Monte Carlo events for $t\bar{t}$ and W+jets, generated as described in Chapter 5, when passed through a fully simulated DØ detector, are found to describe the data quite well [46, 47]. They are therefore used to check the final calibration of the $t\bar{t}$ fitting procedure to correct for an imperfect response.

The same $t\bar{t}$ samples used for the response studies described above are used here as well, except that jets are no longer required to match partons. In addition, the W+jets MC sample described in Chapter 5 is also used to model the background. For each sample and each lepton channel (e+jets and μ+jets), P_{sgn} and P_{bkg} are calculated for 4000 MC events that pass the kinematic selection for $t\bar{t}$. Ensembles are drawn from these event pools, with an ensemble composition same as measured for the data sample (Table 5.1). Each MC ensemble has a fixed total number of events but the number of signal and background events is made to fluctuate around the mean measured $t\bar{t}$ purity. As mentioned previously, another choice for the

fraction of signal/background in the ensembles would be to use the fractions fitted in our ME method, which can be obtained prior to the m_{top} and JES calibrations. The latter choice is expected to be more stable, given the uncertainties in the purities obtained using the topological likelihood fit mentioned in Chapter 5.

Each probability is normalized according to the flavor of the isolated lepton. The multijet contribution is not added during the calibration but treated as a systematic uncertainty (see Section 7.2).

6.4.1 Analysis Ignoring b-tagging

For the analysis that ignores b-tagging information ("untagged" analysis), the calibrations resulting for the fit to the combined e+jets and μ+jets ensembles are shown in Fig. 6.9. The calibration includes a Gaussian prior for the JES parameter, and corresponds to the calibration correction to be applied to $t\bar{t}$ data for the untagged analysis. No attempt is made to measure the JES in this case, because the grid size for steps in JES is not optimal to provide a good calibration. The JES is calibrated and measured only in the b-tagged analysis.

6.4.2 Analysis Relying on b-tagging

For the analysis that incorporates b-tagging, the construction of ensembles has an extra step to determine which of the jets are b-tagged. There are two ways to do this: the same algorithm used to tag jets in all data can be applied to $t\bar{t}$ events, or the TRF used to assign weights to different jet permutations can be applied to tag the jets.

For the final result, the TRF was used as in the previous analysis [53]. However, the direct tagging of MC events was also implemented, and the difference in the result was used as a measure of stability and to estimate the systematic uncertainty

Figure 6.9: Fitted m_{top} and pulls as a function of the input top-quark mass (top mass hypothesis) for ℓ+jets used to calibrate the Matrix Element method when using a Gaussian prior for JES. The studies ignore b-tagging information ("untagged" analysis). The dotted line represents perfect response, and the continuous line is a fit to the results of the ME analysis.

attributable to b-tagging.

Direct Tagging in MC Events

The neural network (NN) algorithm used in this analysis [41, 42] returns a number between 0 and 1 for each jet. The higher the output, the more likely it is that the jet is a b quark. As described previously, we use an NN output of > 0.65 to define any jet as b-tagged. This is the "Medium" operating point.

When used on MC events, the tagging rates are corrected for their 10% larger efficiencies relative to data. To correct for this effect, a random 10% of the MC jets that pass the NN=0.65 cutoff are considered not b-tagged. Only the $t\bar{t}$ signal is treated in this way, while the TRF method is used for the W+jets background.

The results of fits to the ensembles are shown separately for the μ+jets and e+jets samples as a functiono of input top mass in Figs 6.10, and 6.11, and as a function of JES ℓ+jets in Fig. 6.12.   The difference between this response
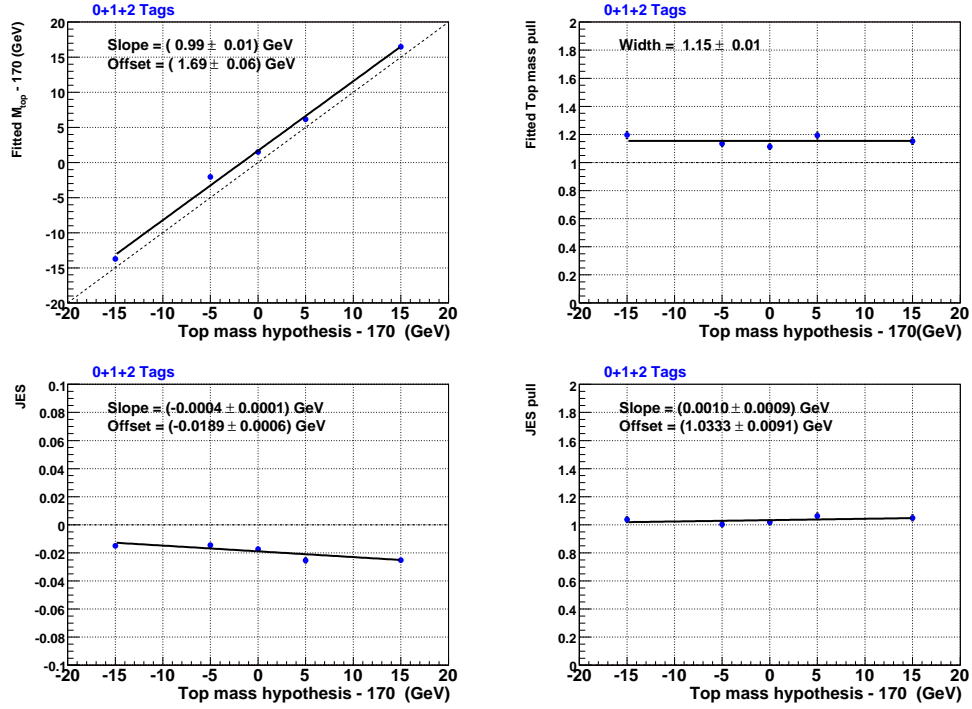
Figure 6.10: Fitted m_{top}, JES and pulls as a function of the input top-quark mass (top mass hypothesis) for μ+jets used to calibrate the Matrix Element method. The studies incorporate b-tagging information, combining events with no tags, 1 tag and 2 or more tags, using direct b-tagging of the $t\bar{t}$ events. The dotted line represents perfect response, and the continuous line is a fit to the results of the ME analysis.

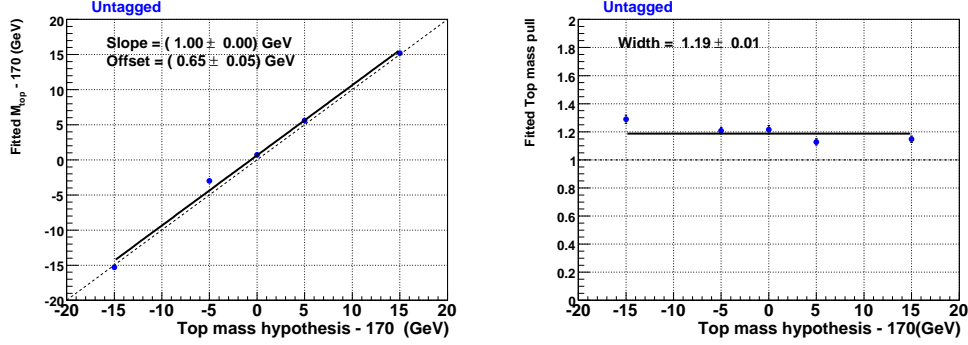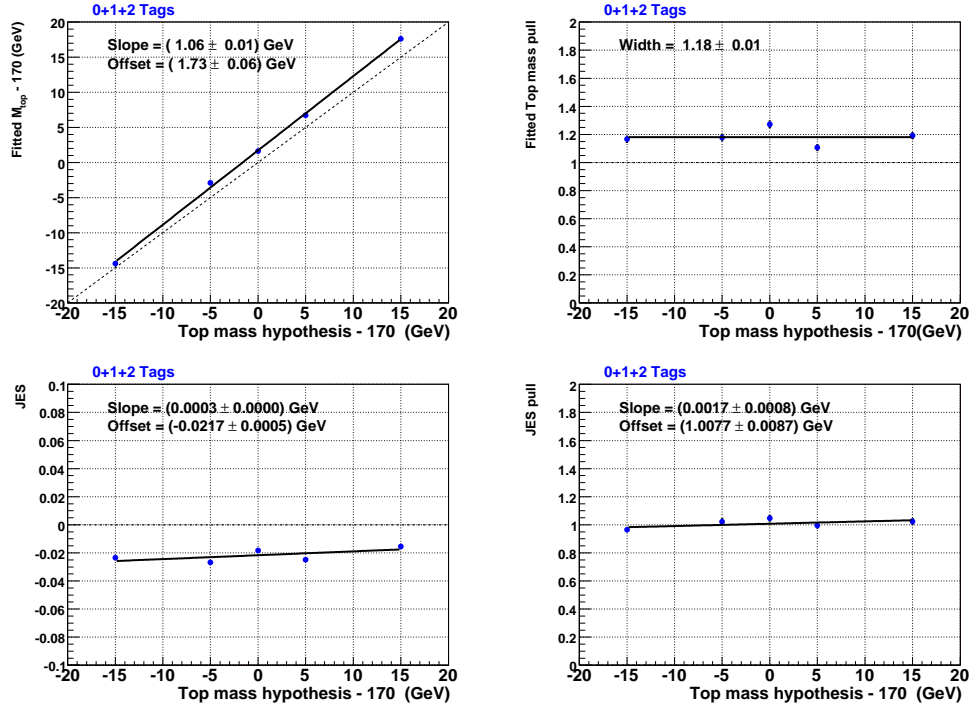Figure 6.11: Fitted m_{top}, JES and pulls as a function of the input top-quark mass (top mass hypothesis) for e+jets used to calibrate the Matrix Element method. The studies incorporate b-tagging information, combining events with no tags, 1 tag and 2 or more tags, using direct b-tagging of the $t\bar{t}$ events. The dotted line represents perfect response, and the continuous line is a fit to the results of the ME analysis.
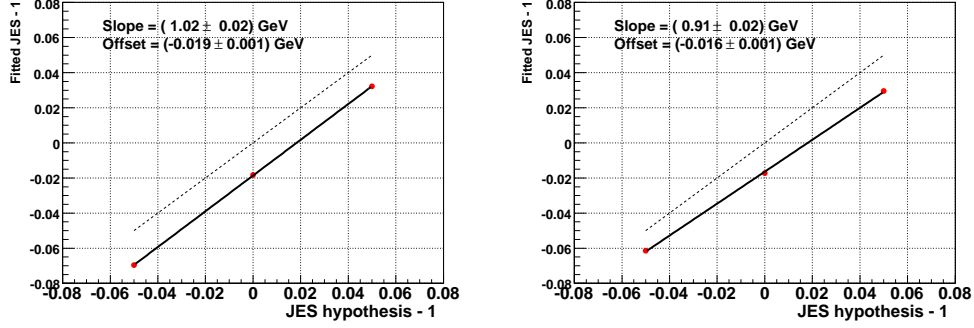
Figure 6.12: Fitted JES as a function of the input JES for e+jets (left) and μ+jets (right) used to calibrate the Matrix Element method. The studies incorporate b-tagging information, combining events with no tags, 1 tag and 2 or more tags, using direct b-tagging of the $t\bar{t}$ events. The dotted line represents perfect response, and the continuous line is a fit to the results of the ME analysis.

and the one below using the TRF method provides an estimate of the systematic uncertainty on b-tagging.

Using Tag-Rate Functions (TRF)

This is the method used to determine the final check of the response of the analysis before applying it to the data. Based on the p_T, η and flavor of each of the jets in generated MC ensembles of events, the TRF provides the per-event probability to have 0, 1 or 2 or more b-taggs. This probability is used on an event-by-event basis to randomly select which jets in the event are to be considered b-tagged in composing the ensembles.

The b-tagged Ensembles

Figure 6.13 shows distributions in the fraction of signal events (purity) for ensembles generated with different number of b-tags (that is, these are not the fitted
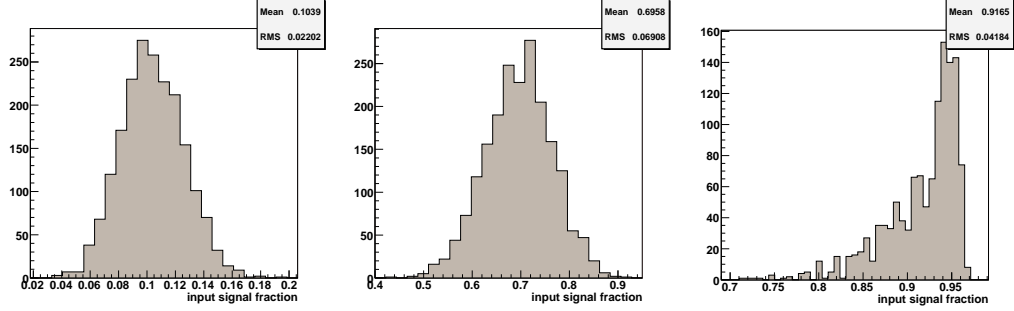
Figure 6.13: Distributions in input $t\bar{t}$ fractions for different b-tagged samples: no b-tags (left), 1 b-tag (center) and 2 or more b-tags (right) per event, and the mean composition of the entire $t\bar{t}$ MC sample.

fractions extracted in the analysis, but the input fractions that define the ensembles). Figure 6.14 summarizes the mean fractions of signal events in ensembles with different number of b-tags per event.

Response as a Function of Number of b-Tags in a Sample

Figure 6.15 shows the response in mass for each subsample for e+jets and Fig 6.16 shows the results for μ+jets. For no tags and for the μ+jets in particular, the result requiere large corrections. This is understandable, considering that the average signal to background ratio is of $\approx$10%. However, this does not constitute a problem, as long as the low-statistics no-tags sample is not calibrated independently. Combining the three samples avoids calibrating low-statistics samples individually before combining the results.

Response for the Combined 0, 1 and 2 tags samples

This is the MC response used for correcting the fit to data. As described before, the 2D likelihoods (involving m_{top} and JES) for the 0, 1 and 2 b-tags are generated
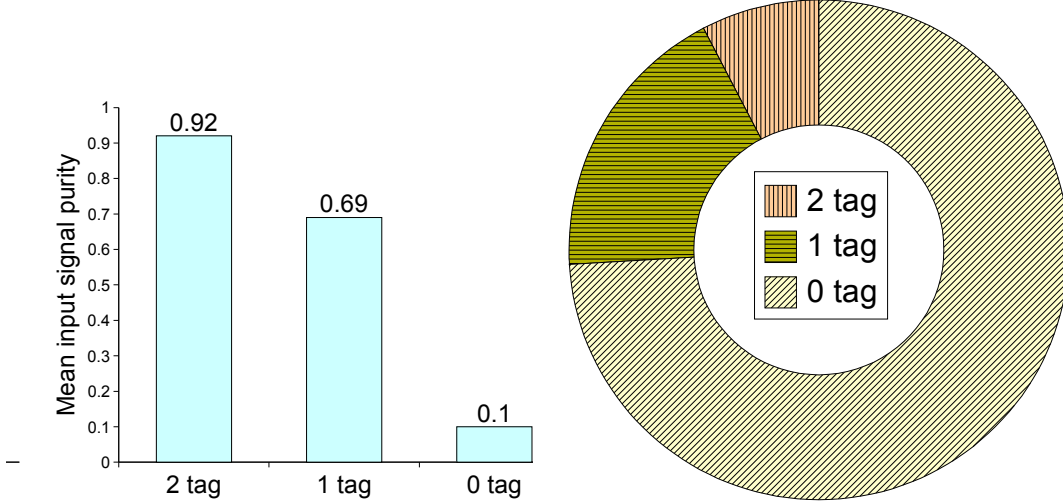
Figure 6.14: Mean input $t\bar{t}$ purity for the different b-tagged samples (left) and the mean sample composition for the entire MC $t\bar{t}$ sample (right).

from the likelihoods given by Eq. 6.26 by evaluating each point in the $(m_{\text{top}}, \text{JES})$ 2D grid to determine the most likely value of the top fraction ($f_{\text{top}}^{\text{best}}$). These three 2D likelihoods are then multiplied together, combining the MC results from the three samples, but separately for e+jets and μ+jets.

This study is done in two steps: first, the response in mass and JES is obtained using a flat JES prior (i.e not yet the Gaussian prior at this point). By definition, a Gaussian prior centered at JES$= 1$ does not shift the mass nor the JES when the method is properly corrected by the response. However, uncertainties are reduced through the prior, and the pull analysis is therefore redone to assess the effect of the prior.

The same procedure is performed for data, with the prior applied after correcting m_{top} and JES using Figs. 6.17-6.19 (see below).

The fit to the results from the ensembles are shown separately for the e+jets and μ+jets samples in Figs. 6.17, 6.18, and 6.19, when JES is not constrained (i.e.,
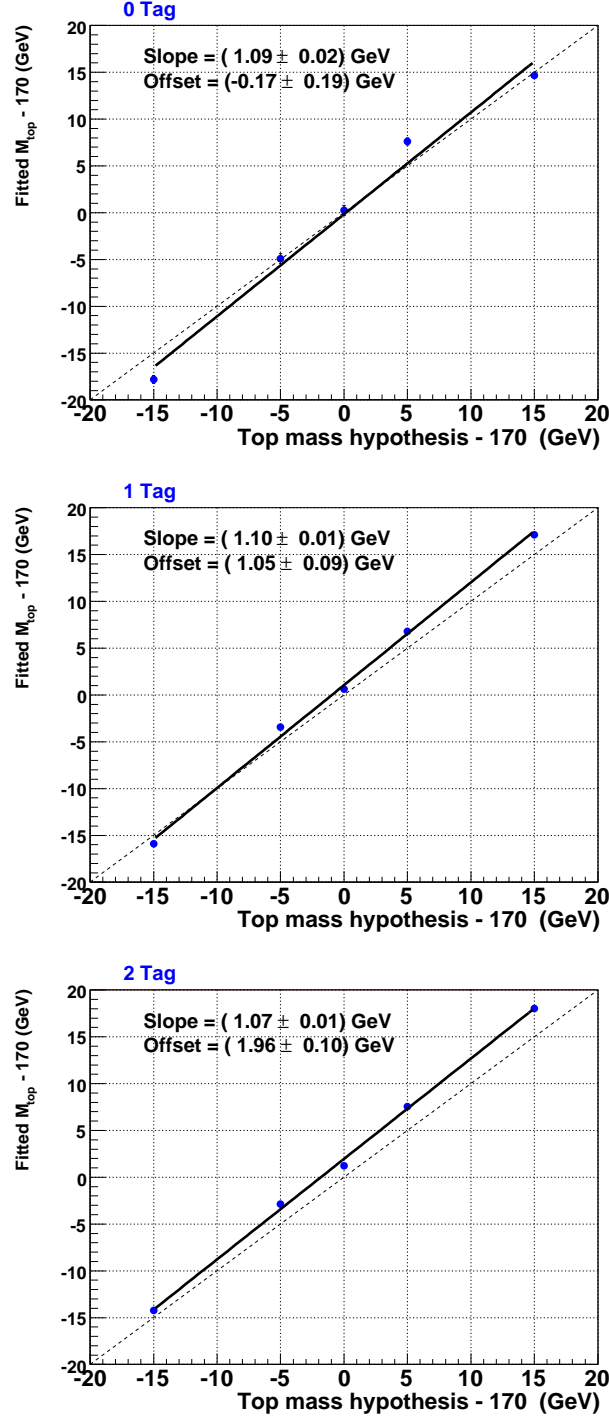
Figure 6.15: Response in mass for the Matrix Element method for e+jets events in the b-tagging analysis, shown as a function of the input top-quark mass, separately for the 0, 1 and 2 or more b-tags samples in (top), (middle) and (bottom), respectively. The dotted line represents perfect response, and the continuous line is a fit to the results of the ME analysis.
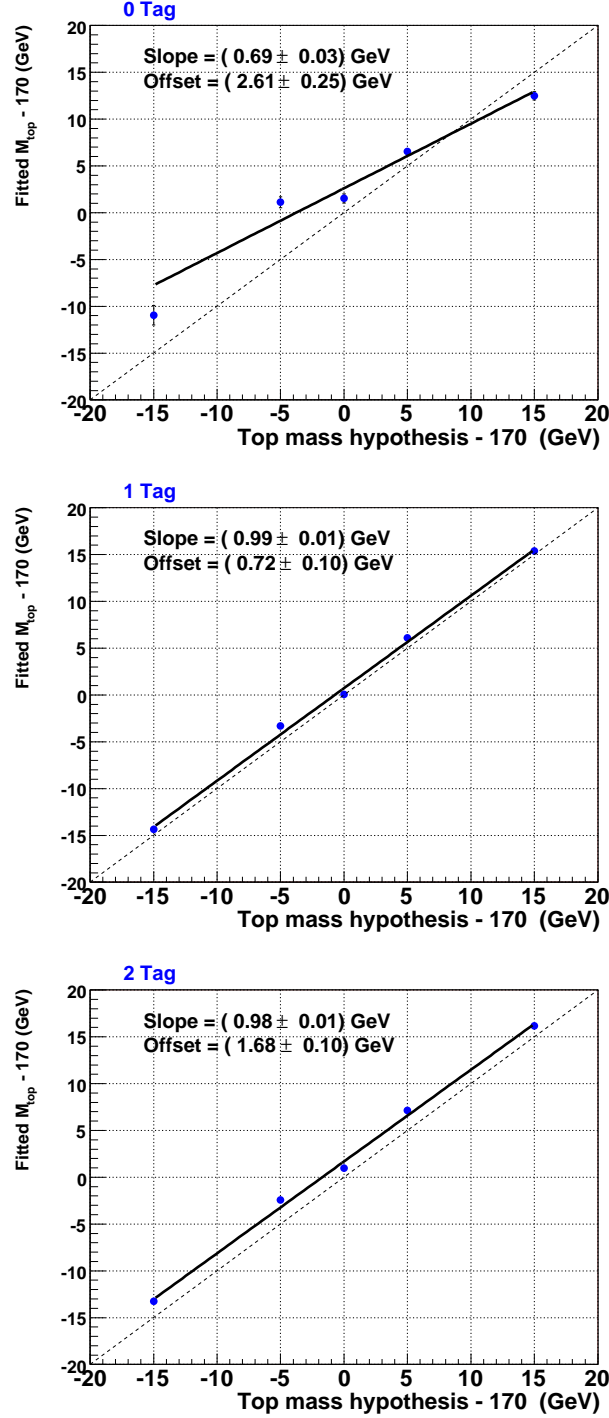
Figure 6.16: Response in mass for the Matrix Element method for μ+jets events in the b-tagging analysis, shown as a function of the input top-quark mass, separately for the 0, 1 and 2 or more b-tags samples in (top), (middle) and (bottom), respectively. The dotted line represents perfect response, and the continuous line is a fit to the results of the ME analysis.
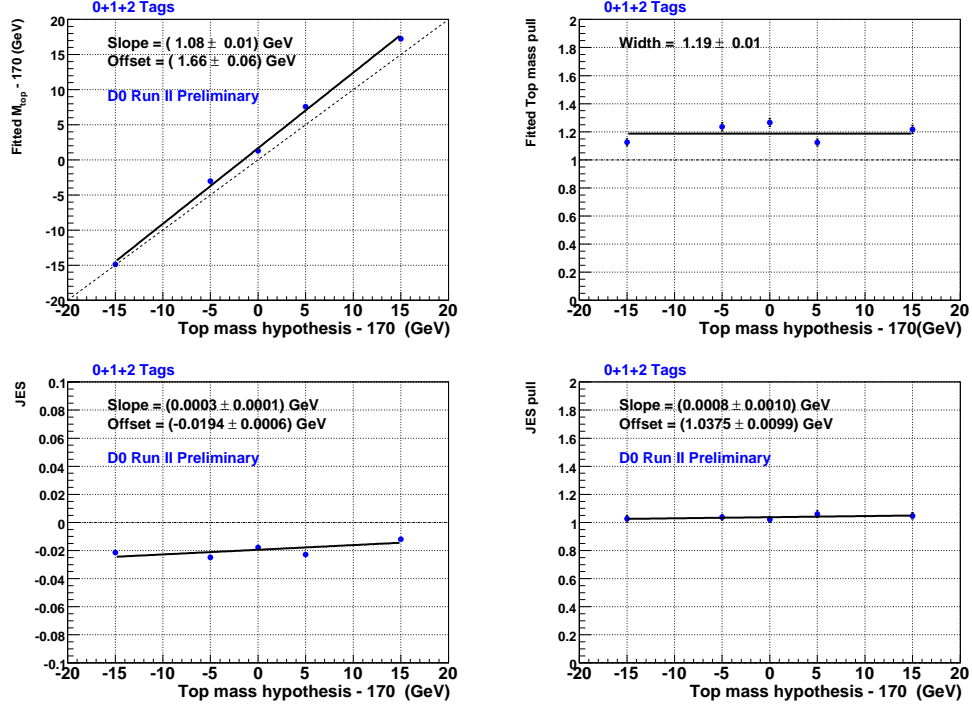
Figure 6.17: Response in mass, JES, and pulls for the Matrix Element method for e+jets events in the b-tagging analysis, combining the 0, 1 and 2 or more b-tags samples, shown as a function of the input top-quark mass, when the JES is unconstrained (i.e., flat prior in JES). The dotted line represents perfect response, and the continuous line is a fit to the results of the ME analysis.

flat prior). (These fits provide the corrections to the data.) After applying the Gaussian prior in JES described previously, the pull distribution improves slightly as seen in Fig. 6.20.
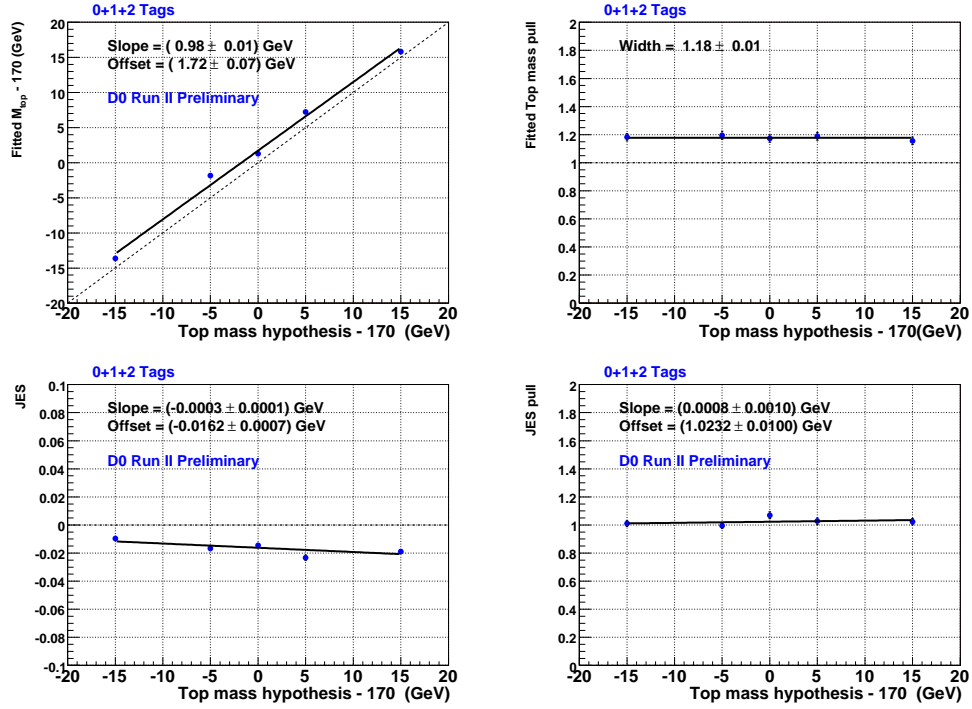
Figure 6.18: Response in mass, JES, and pulls for the Matrix Element method for μ+jets events in the b-tagging analysis, combining the 0, 1 and 2 or more b-tags samples, shown as a function of the input top-quark mass, when the JES is unconstrained (i.e., flat prior in JES). The dotted line represents perfect response, and the continuous line is a fit to the results of the ME analysis.
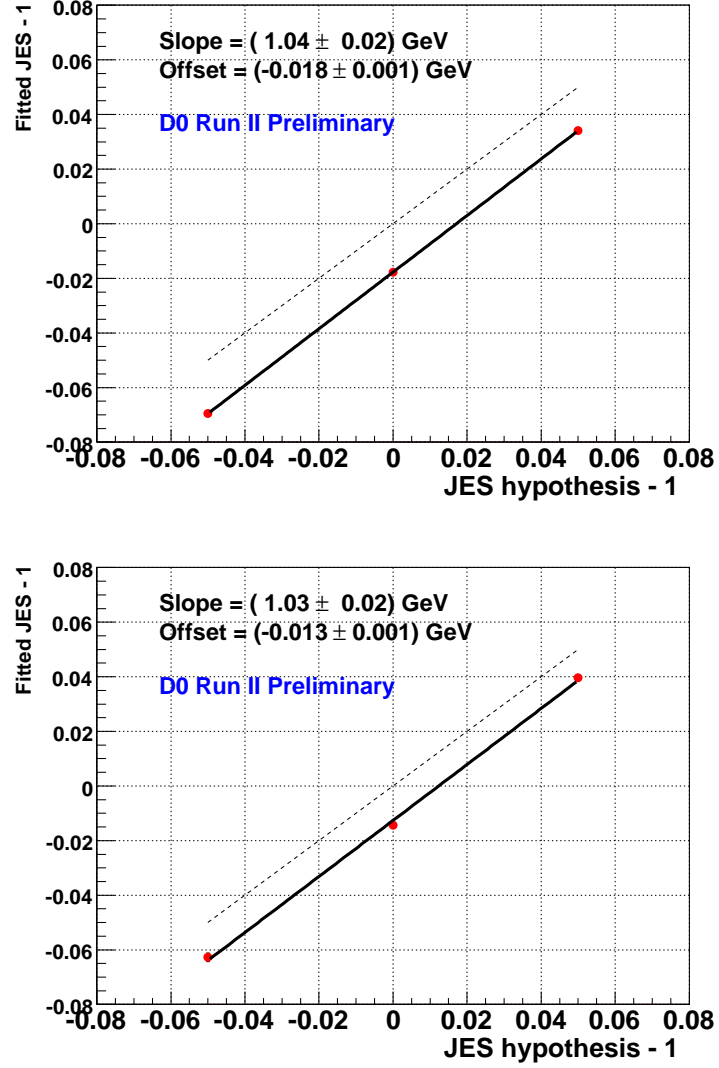
Figure 6.19: Response in JES for the Matrix Element method for e+jets (top) and μ+jets (bottom) events in the b-tagging analysis combining the 0, 1 and 2 or more b-tags samples, shown as a function of the input JES when the JES is unconstrained (i.e., flat prior in JES). The dotted line represents perfect response, and the continuous line is a fit to the results of the ME analysis.
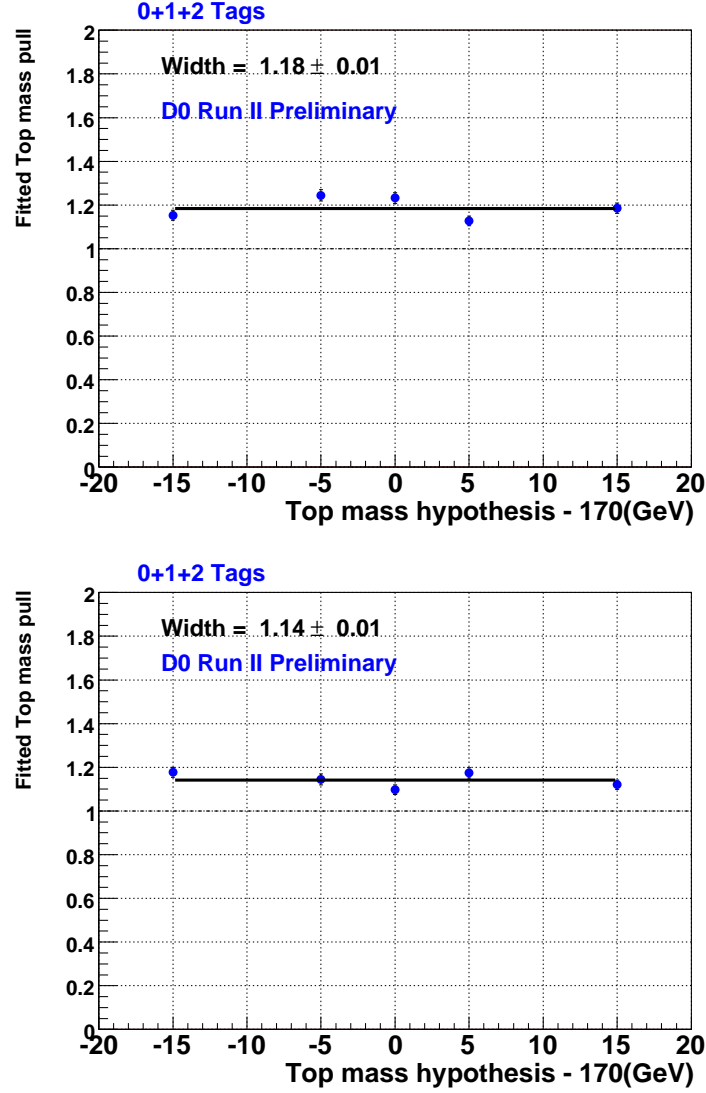
Figure 6.20: Pull widths after applying the Gaussian prior to the corrected sample for e+jets (top) and μ+jets (bottom) events in the b-tagging analysis, combining the 0, 1 and 2 or more b-tags samples, shown as a function of the input top-quark mass. The dotted line represents perfect response, and the continuous line is a fit to the results of the ME analysis.

Chapter 7

Analysis of the Data

In this chapter we present the results of applying the Matrix Element method to data. Unless stated otherwise, the MC studies of the response in the mass and JES presented in the previous chapter, are used to correct the response in data. We present results ignoring as well as using b-tagging information. For the analysis with b-tagging we present results with and without the implementation of a Gaussian prior in JES (based on the independent measurement in γ+jets data). At the end of the chapter, we show studies on the systematic uncertainties that affect this analysis.

7.1   Results for Mass and JES

The Matrix Element method is applied to the 913 events/pb e+jets and the 871 events/pb μ+jets data samples, using corrections for m_{top} and JES found in the previous chapter.

7.1.1 Results when b-tagging Information is Ignored

The results of fits to the 2D likelihood for the combined ℓ+jets sample for the untagged analysis, and using a Gaussian prior in JES are shown in Fig. 7.1. As indicated above, only the results for m_{top} and its uncertainty δm_{top} are corrected and no correction is applied to the results for JES for the reasons discussed in Section 6.4. The fitted uncertainty is inflated by a factor of 1.19 to account for the larger standard deviation (SD) of the pulls in mass, as determined from the study in Fig. 6.9.

For the untagged analysis, the top mass is measured to be:

$$m_{\text{top}}^{\ell+\text{jets}}(\text{untagged}) \quad = \quad 171.1 \pm 3.0(\text{stat \& JES})\text{GeV}$$

$$(7.1)$$

Figure 7.2 shows the expected distribution of fitted uncertainties in m_{top} extracted from a mix of signal and background MC for $t\bar{t}$ events generated with $m_{\text{top}} = 170$ GeV. We see that the δm_{top} extracted from data is smaller than expected, but not exceedingly unlikely ($\approx$6% probability). The uncertainty reflects contributions from statistics of the sample, the uncertainty in JES and its correlation with m_{top} (see below).

7.1.2 Results when Using b-tagging Information

Results for the b-tagged analysis are shown separately for the e+jets and μ+jets channels in Fig. 7.3 and Fig. 7.4 for the 0+1+2 tag samples, using a flat prior in JES. The resolution in the e+jets is somewhat better than for μ+jets, as expected because of the larger number of events, the purity of the sample and better resolution in measuring electron momentum. The differences in the mass and JES

$m_{top} = (171.1 \pm^{3.0}_{3.0})$ (stat.) GeV

Likelihood

900pb^{-1}
Untagged
504 Events

Reconstructed mass (GeV)

JES = $(1.025 \pm^{0.023}_{0.023})$ (stat.)

Likelihood

D0 Run II Preliminary

900pb^{-1}
Untagged
504 Events

JES
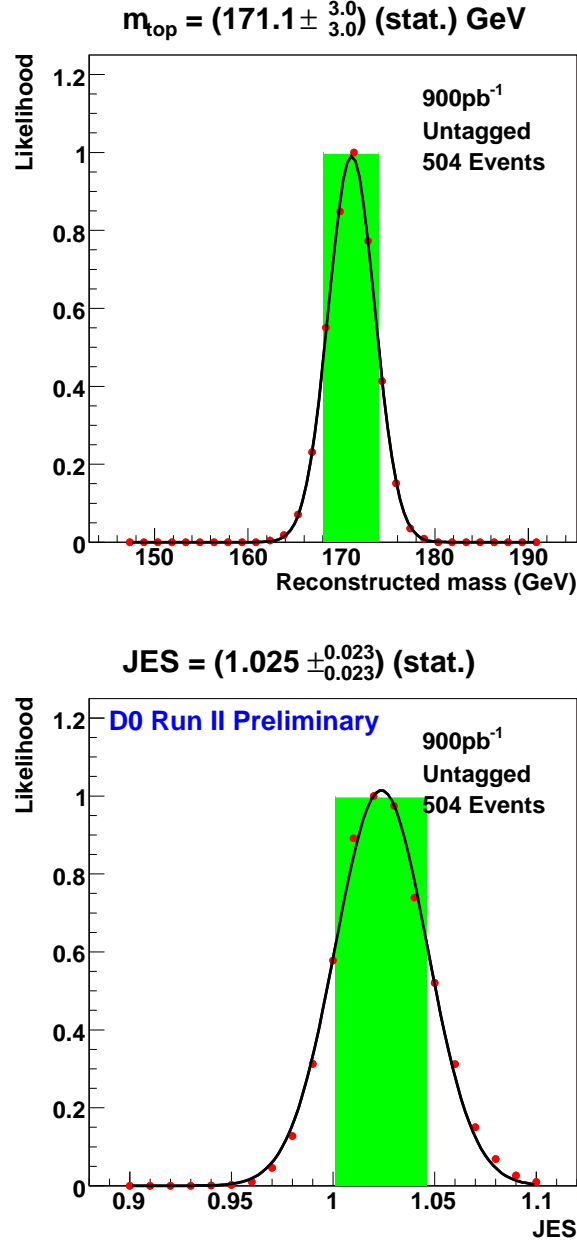
Figure 7.1: Application of the Matrix Element method to the combined ℓ+jets data when b-tagging information is ignored ("untagged" analysis), using a Gaussian prior in JES. The top plot shows the probability as a function of assumed m_{top}. The m_{top} axis corresponds to already corrected values. The bottom plot shows the probability as a function of JES, with the JES axis not corrected, and a flat prior on JES.

Figure 7.2: Distribution of fitted uncertainties obtained from MC ensembles of W+jets and $t\bar{t}$ events for the m_{top} =170 GeV sample. This is used to check the the analysis of the combined ℓ+jets channel, without using b-tagging information, and a Gaussian prior for JES is applied. The uncertainty found in data is indicated by the arrow. All uncertainties have been inflated by the width of the pull for the mass distributions.
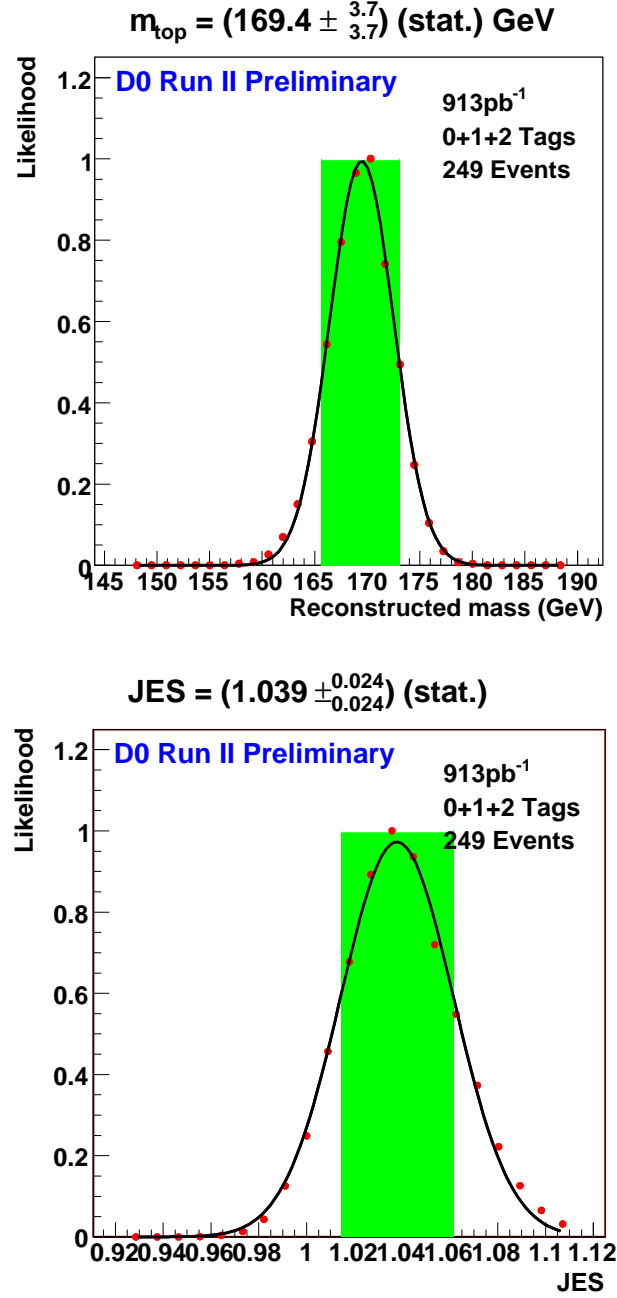
Figure 7.3: Application of the Matrix Element method to e+jets data using b-tagging information and using a flat prior in JES. The top plot shows the probability as a function of assumed m_{top}. The bottom plot shows the probability as a function of JES. The m_{top} and JES axes correspond to their corrected values from MC. The shaded region denotes the 68% of area, and the probabilities are normalized to have the maximum point at 1.

$m_{top} = (169.0 \pm {}^{3.9}_{3.9})$ (stat.) GeV

Likelihood

1.2

D0 Run II Preliminary

871pb^{-1}
0+1+2 Tags
255 Events

1

0.8

0.6

0.4

0.2

0

150   160   170   180   190

Reconstructed mass (GeV)

$JES = (1.052 \pm {}^{0.023}_{0.023})$ (stat.)

Likelihood

1.2

D0 Run II Preliminary

1

871pb^{-1}
0+1+2 Tags
255 Events

0.8

0.6

0.4

0.2

0

0.92 0.94 0.96 0.98 1 1.02 1.04 1.06 1.08 1.1 1.12

JES
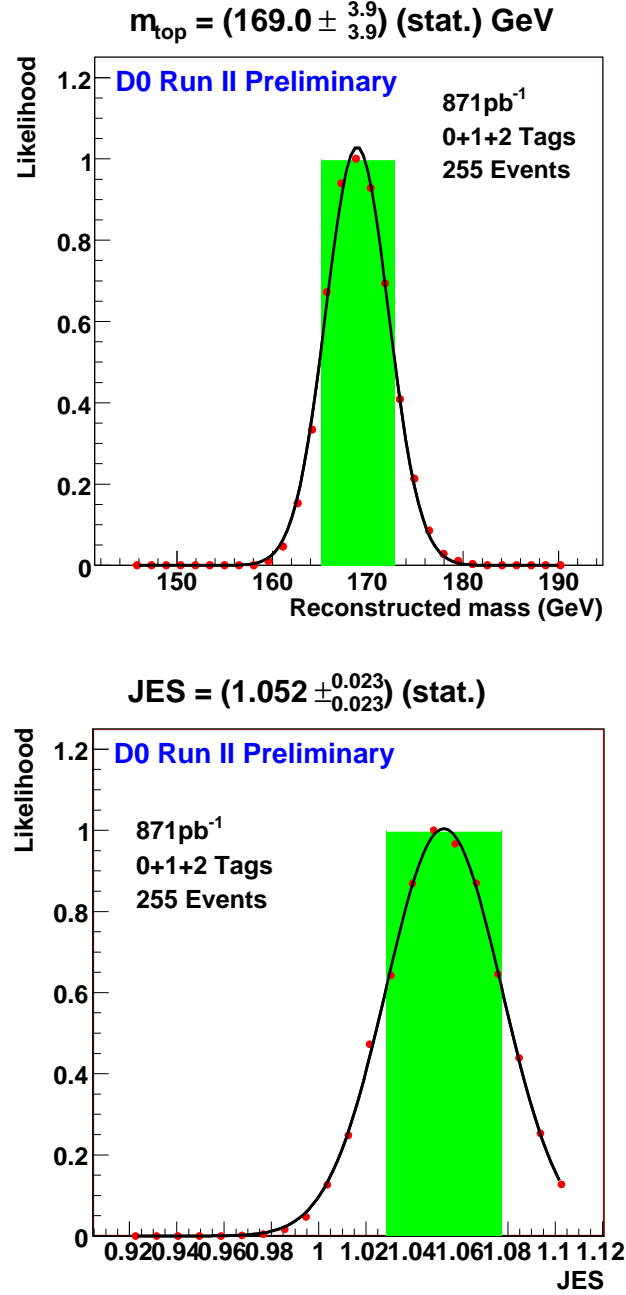
Figure 7.4: Application of the Matrix Element method to μ+jets data using b-tagging information and using a flat prior in JES. The top plot shows the probability as a function of assumed m_{top}. The bottom plot shows the probability as a function of JES. The m_{top} and JES axes correspond to their corrected values from MC. The shaded region, denotes the 68% of area and the probabilities are normalized to have the maximum point at 1.
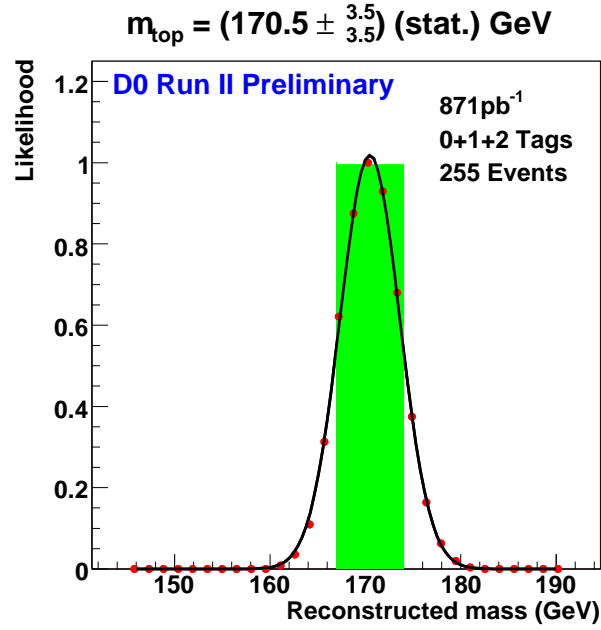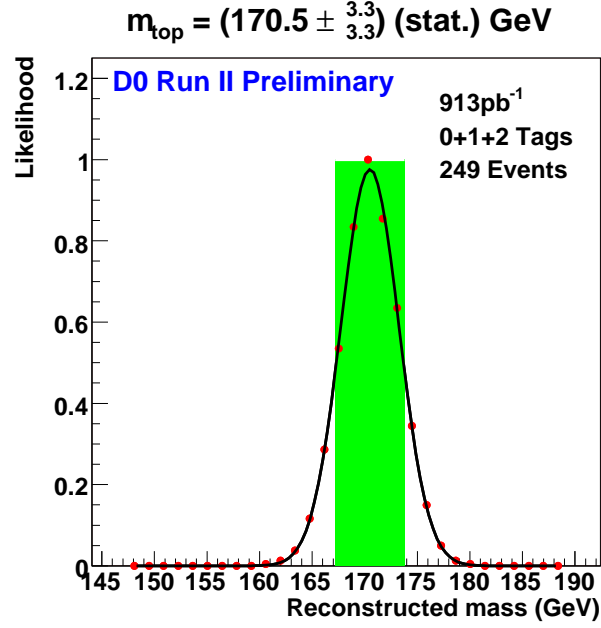
Figure 7.5: Application of the Matrix Element method to e+jets (top) and μ+jets (bottom) data using b-tagging information and when using a Gaussian prior in JES. The plots shows the probability as a function of assumed m_{top}. The m_{top} axes correspond to their corrected values from MC. The shaded region denotes the 68% of area, and the probabilities are normalized to have the maximum point at 1.
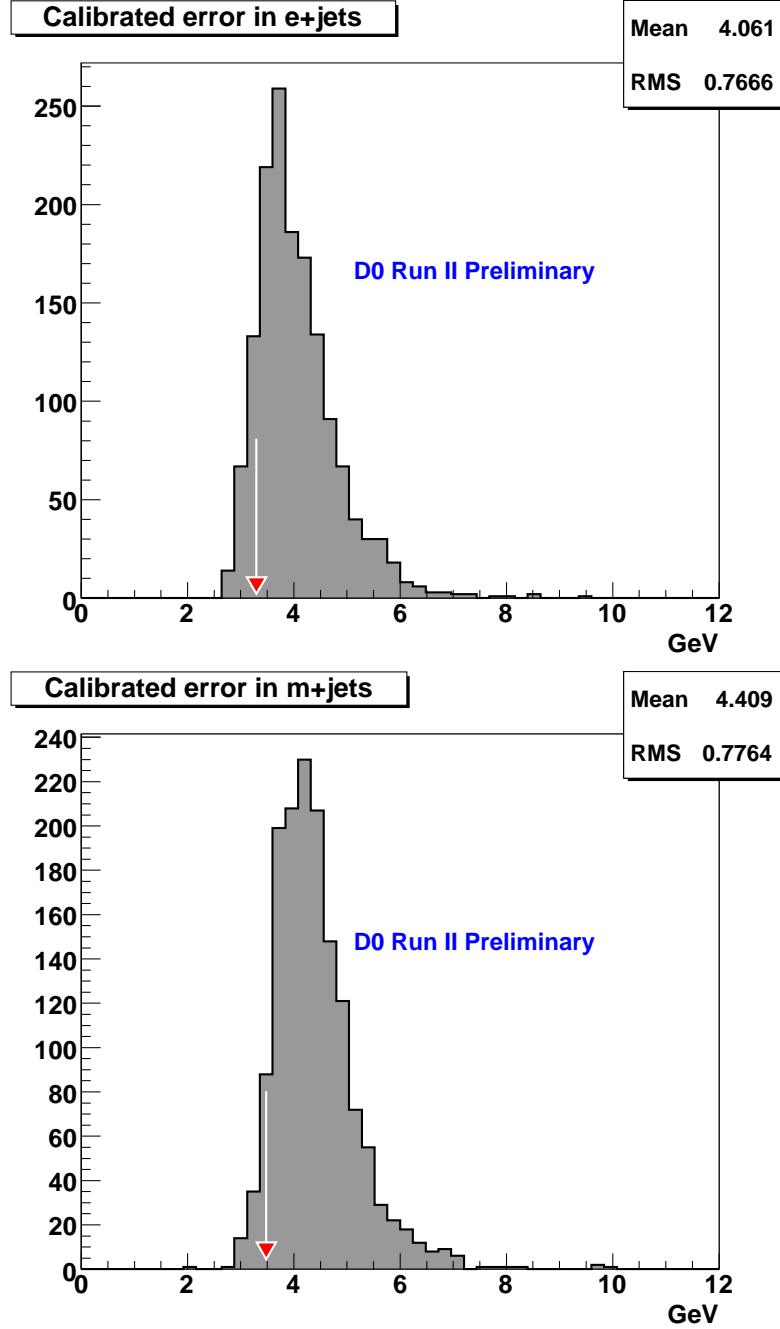
Figure 7.6: Distribution of fitted uncertainties obtained from MC ensembles of W+jets and $t\bar{t}$ events for m_{top} =170 GeV, used to check the mass calibration of the analysis in the e+jets channel (top) and μ+jets channel (bottom), using b-tagging information and a Gaussian prior for JES. The uncertainty found in data is indicated by the arrow. All uncertainties have been inflated by the widths of the pulls in the mass.

between the two channels are compatible with the uncertainties.

The results when a Gaussian prior for JES is used are shown in Fig. 7.5. Applying the Gaussian prior, reduces the uncertainty in the mass by $\approx 10\%$. Also, the difference in extrated mass between the two channels is reduced to < 0.1 GeV as a result of applying the Gaussian prior in JES. A comparison between the expected uncertainty from MC tests and the measured uncertainty in data is shown in Fig. 7.6 separately for e+jets and μ+jets. Similarly to the analysis ignoring b-tagging, the δm_{top} extracted from data is smaller than expected, $\approx 10\%$ probability in the e+jets, and $\approx 7\%$ probability in the μ+jets channel. For the b-tagged analysis, the measured top mass for the $0+1+2$ samples after applying a Gaussian prior in JES are:

$$
\begin{aligned}
m_{\text{top}}^{e+\text{jets}}(b-\text{tag},\ 0+1+2) &= 170.5 \pm 3.3(\text{stat} + \text{JES})\text{GeV}; \\
m_{\text{top}}^{\mu+\text{jets}}(b-\text{tag},\ 0+1+2) &= 170.5 \pm 3.5(\text{stat} + \text{JES})\text{GeV}; \\
m_{\text{top}}^{\ell+\text{jets}}(b-\text{tag},\ 0+1+2) &= 170.5 \pm 2.4(\text{stat} + \text{JES})\text{GeV}.
\end{aligned}
$$

$$(7.2)$$

Figure 7.7 shows the expected distribution in uncertainties for the combined ℓ+jets sample from W+jets and $t\bar{t}$ MC events. The arrow marks the uncertainty observed in the combined ℓ+jets data when the Gaussian prior in JES is used in the analysis with b-tagging.

For completeness, Fig. 7.8 shows the corrected final two dimensional (JES vs m_{top}) contours of equal probability for the likelihoods (using the Gaussian prior), for e+jets and μ+jets data. The top mass and JES values and their uncertainties are extracted by projecting these distributions onto the respective axis.
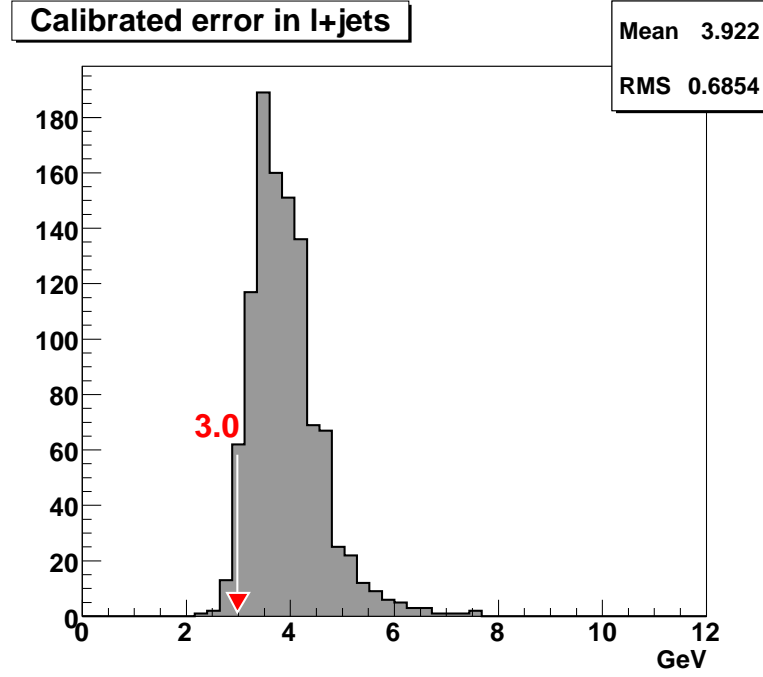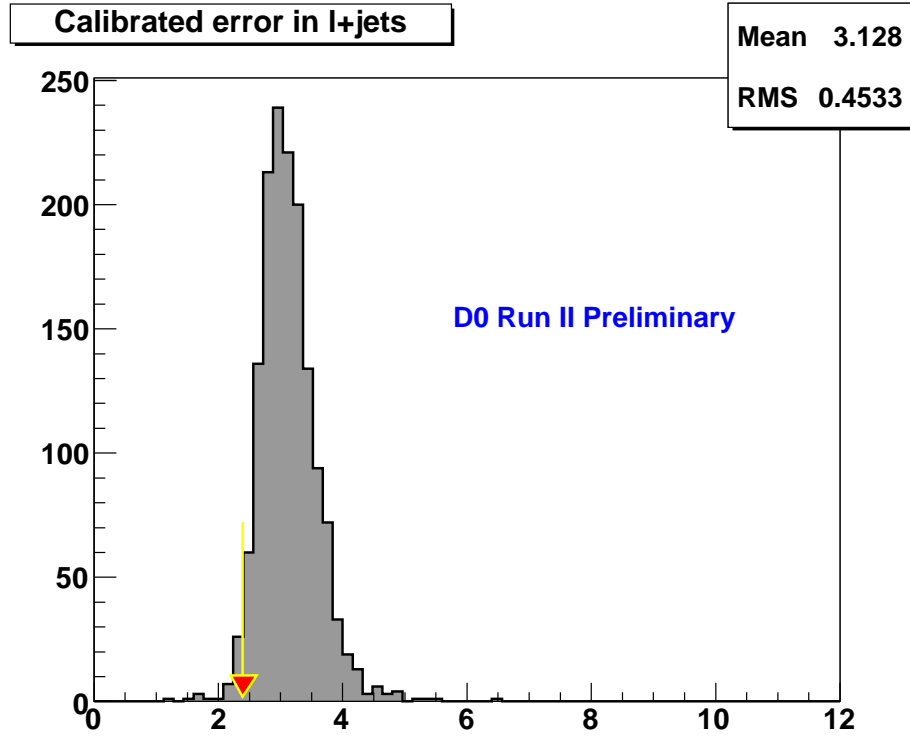
Figure 7.7: Distribution of fitted uncertainties obtained from MC ensembles for the m_{top} =170 GeV sample used to check the mass response for the analysis of the combined ℓ+jets channel, using b-tagging information, when a Gaussian prior for JES is applied. The uncertainty found in data is indicated by the arrow. All uncertainties have been inflated by the width of the pull for the mass distributions.
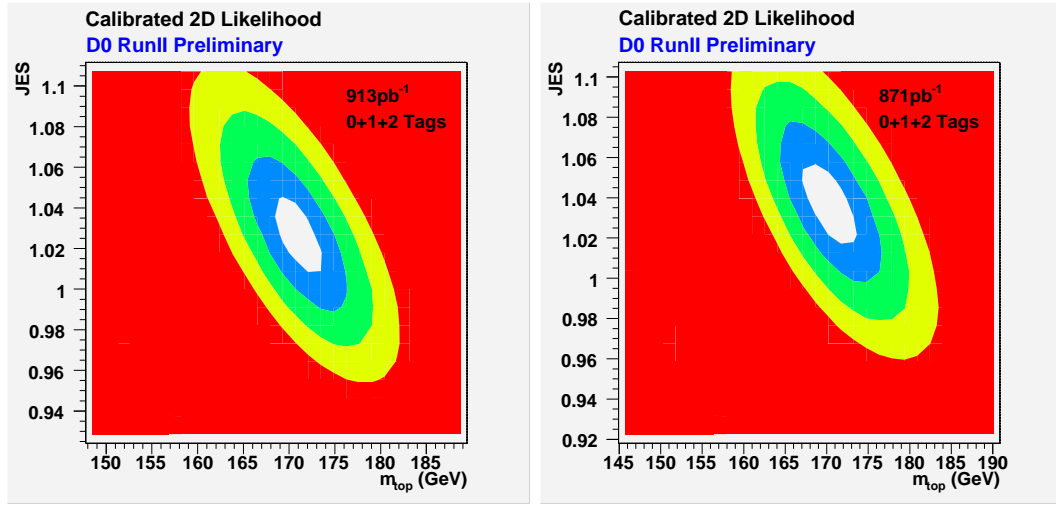
Figure 7.8: Two dimensional likelihoods from the analysis of the e + jets (left), and μ + jets (right) using b-tagging information and a Gaussian prior for JES. The shadings show one SD contours in probability, with the mass and JES axis corresponding to their corrected values.

7.2   Systematic Uncertainties

Despite the effort to account for assumptions made in the calculation of the probabilities, there are uncertainties in the measurement of m_{top} from possible differences between data and MC and from the ME method itself.

Systematic uncertainties can be group in three sources: modeling of the processes for $t\bar{t}$ production and background, modeling of the detector performance, and uncertainties inherent in the method of analysis. The recognized uncertainties are summarized in Table 7.1. The three dominant sources correspond to modeling of signal, modeling of b fragmentation and response of the calorimeter to remnants of b-quarks as opposed to light quarks. The systematic uncertainty on the jet energy scale was at one point the dominant concern, and is now included in the Bayesian procedure discussed in the previous section. Assuming no correlations, the total systematic uncertainty on the measured top mass is obtained by adding all contributions in quadrature. (The correlation between m_{top} and JES is already accounted for in the 2D analysis.) Unless indicated to the contrary, the procedure to evaluate systematic uncertainties is to quantify a change in the mass response by re-doing the analysis of MC ensembles for $t\bar{t}$ events generated at $m_{\text{top}} = 170$ GeV, using a different assumption for any subprocess that can impact the measurement.

7.2.1   Modeling the Physical Processes

Modeling Signal

The Monte Carlo $t\bar{t}$ signal events used for checking the method were generated with PYTHIA using the default set of parameters named "Tune A." To estimate the systematic effect on m_{top} arising from uncertainties in modeling signal, a second sample was generated with PYTHIA, using a different set of parameters "Tune

Source of Uncertainty	Untagged Analysis	b Tagging Analysis
statistical and jet energy scale	± 3.0	± 2.4
modeling of process:		
signal	± 0.98	± 0.45
background	± 0.47	± 0.15
Wbb+jets content	± 0.24	± 0.24
PDF uncertainty	$+0.26\ -0.40$	$+0.16\ -0.39$
b fragmentation	± 0.14	± 0.54
b/c semileptonic decays	$+0.06\ -0.07$	± 0.05
modeling of detector:		
JES p_T dependence	± 0.14	± 0.23
b response in calorimeter	± 0.71	± 0.57
trigger	± 0.08	± 0.08
ME method:		
signal fraction	± 0.15	$+0.53\ -0.24$
multijet contamination	± 0.16	± 0.21
MC JES and m_{top} corrections	± 0.06	± 0.07
b-tagging		± 0.29
total systematic uncertainty	± 1.4	± 1.2
total uncertainty	± 3.3	± 2.7

Table 7.1: Summary of uncertainties on the top-quark mass, with values quoted in GeV.

DW." Both PYTHIA Tunes are described in Ref. [57]. Tune DW includes an alternative modeling of the underlying event and initial and final-state radiation. The top-mass measurement is sensitive to gluon radiaton, either because the additional jets can be confused with those coming from top or antitop decay, or because the energy loss to soft radiation is not considered in a leading-order scheme for $\mathcal{M}$. The effect is minimized by requiring events with exactly four jets in the final state. Nevertheless, when jets from decay products are lost, they can be replaced by initial or final-state radiation, causing bias. Studies in mass response were performed on both Tune A and Tune DW samples for $m_{\text{top}} = 170$ GeV, and the difference in the mean fitted m_{top} values between the two samples defined as systematic uncertainty.

Modeling Background

To study the effect of the choice of background model on the measurement of the top mass, the standard W+jets Monte Carlo sample is reweighted to simulate the effect of using alternative factorization scales in the generation of these events [58]. The study of MC ensembles with $m_{\text{top}} = 170$ GeV used to check the method is repeated using the reweighted W+jets events, and the difference in the fitted m_{top} compared with that using the default weights is defined as systematic uncertainty.

Wbb+jets Content

Because of limitations in CPU time only W+light jets was used as background, ignoring heavy flavor content. To estimate the effect of this simplification, we evaluate the shift in fitted m_{top} in MC ensembles with $m_{\text{top}} = 170$ GeV, in the e+jets channel, when heavy flavor is added in the expected amounts. Behavior in the μ+jets channel is assumed to be same as in e+jets.

Uncertainty from Choice of PDF

To calculate P_{sgn} and P_{bkg} we use leading-order matrix elements, and both calculations utilize leading-order parton distribution functions (PDF) [59]. To estimate the systematic uncertainty on m_{top} from this choice, the difference provided using the next-to-leading-order PDF CTEQ6M [60] is used for this systematic uncertainty. This uncertainty is taken from the previous m_{top} analysis [53].

Model for Fragmentation of the b-quark

The overall uncertainty on the jet energy scale JES is included in the uncertainty in the 2D fit of the likelihood in the (JES,m_{top}) plane. The differences in the response to b and light jets are considered through the transfer functions obtained from simulation. However, differences between data and simulation can affect the measurement. We studied possible effects of such differences by reweighting MC $t\bar{t}$ events to simulate other choices of fragmentation of b jets. The $t\bar{t}$ events for $m_{top} = 170$ GeV, generated using the Bowler default scheme [61], were reweighted according to the ALEPH, DELPHI, and OPAL tune (ADO) [63]. Studies of MC ensembles were repeated using the reweighted events, and the difference in the fitted m_{top} was taken as a systematic uncertainty on b fragmentation.

Semileptonic Decays of b/c quarks

The reconstructed energy of b jets containing semileptonic bottom or charm decays is in general lower than that of b jets containing only hadronic decays. This can be taken into account only for jets in which a soft muon is reconstructed and the fitted top-quark mass must therefore depend on the semileptonic b and c decay branching fractions. These fractions were varied within the bounds given in Ref. [64], and found to have a small effect. The systematic uncertainty from this source is taken

from the previous m_{top} analysis [53].

7.2.2 Modeling the Detector

Dependence of JES on p_{T}

The relative difference between the jet energy scale in data and Monte Carlo is obtained through a global scaling factor (JES) using the known W mass as a constraint. The corresponding uncertainty on m_{top} is included in the quoted result (stat. & JES). Any discrepancy between data and simulation other than a global difference in scale can lead to additional uncertainty on the top-quark mass. To estimate this effect, the energies of all jets in data were re-scaled by a factor corresponding to the uncertainty in JES, which depends on the energy E and pseudorapidity η of the jet, according to a parametrization in E and η (see Fig. 7.9) determined from jets in the $m_{\text{top}} = 170$ GeV Monte Carlo sample used for checking the ME analysis. The difference in the fitted m_{top} between the modified and standard JES is taken as the systematic uncertainty.

Relative JES for b and Light Jets

In addition to differences in JES for b jets between data and simulation that arise from different modeling of b fragmentation (see above), variations in response of the two parts of calorimeter (electromagnetic and hadronic) can also lead to such discrepancies. This difference in JES is estimated to be $\approx 1.5\%$. A MC ensemble of ≈ 2000 events was formed using the standard $m_{\text{top}} = 170$GeV $t\bar{t}$ MC sample. This was analyzed using the default values for JES, and re-analyzed with the b jets re-scaled by 1.5% in energy. The difference in the fitted m_{top} for the two analyses was taken as systematic uncertainty.
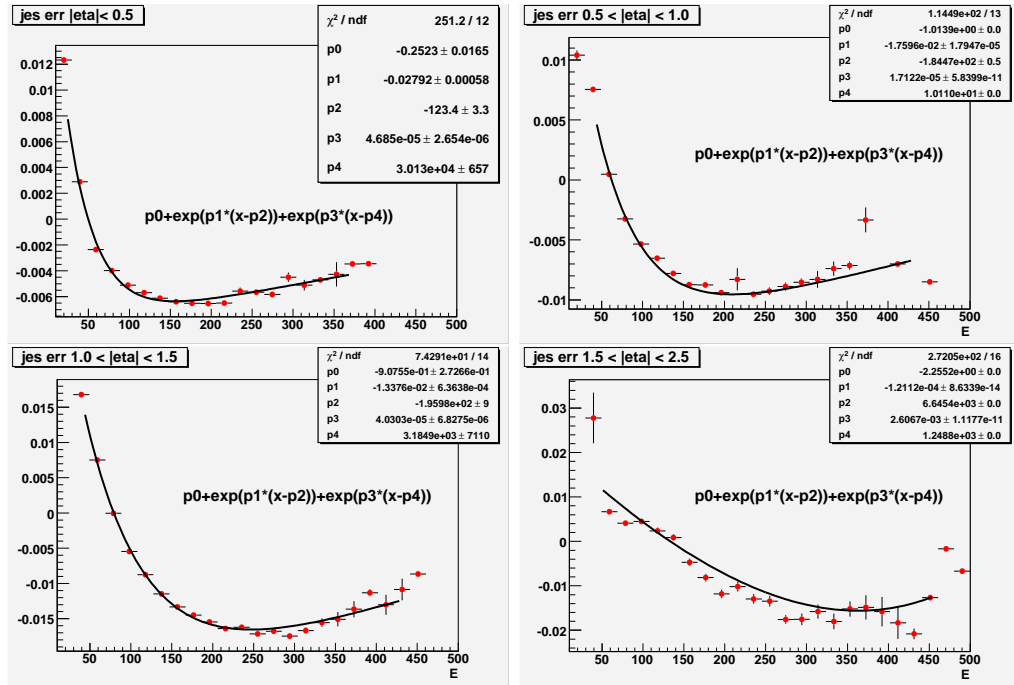
Figure 7.9: Parameterization of 1 standard-deviation uncertainty in jet energy scales as a function of jet energies E, for four η regions, determined from jets in the $m_{\text{top}} = 170$ GeV Monte Carlo sample used to check the ME analysis.

Trigger Efficiencies

The trigger efficiencies used in forming ensembles for checking the measurement are varied within their uncertainties, and provided uncertainties δm_{top}. We quote the result from the previous analysis [53].

7.2.3 Uncertainties Related to Choice of Method of Analysis

Dependence of Corrections to m_{top} from Assumed Signal Fraction

We use the signal fractions from the sample composition determined in a likelihood fit to the data that ignored b-tagging. Because the uncertainties on these fractions are not insignificant, the analysis of the response is repeated by varying these fractions within the uncertainties determined in the fit. The difference in the top mass is then taken as systematic uncertainty. This small systematic uncertainty can be reduced using the fractions measured with the full Matrix Element method, and can be contemplated in the future.

Multijet Background

We used simulated $W+$jets events to model the small multijet ("QCD") background in the data. To estimate the effect of this assumption, we selected a QCD-enriched sample of events from data by inverting the lepton-isolation requirement in selecting the events (i.e., requiring a not isolated lepton instead of an isolated one). The studies using MC ensembles for $m_{\text{top}} = 170$ GeV were repeated including this QCD-enriched sample. The difference in the fitted m_{top} when this background sample is included is taken as the systematic uncertainty from ignoring the multijet background in the model.

Response of Analysis to Input m_{top} and JES

This systematic uncertainty is estimated by varying the correction to the top mass extracted from data according to the uncertainties of the fits shown in Figs. 6.17, 6.18 and 6.19. The difference in the mass result from changing the mass response is added in quadrature to the change in the mass from a change in JES response, and the resultant quoted as systematic uncertainty.

b-tagging

For obtaining the systematic uncertainty from b-tagging, the entire MC analysis was redone using the b-tagging NN algorithm rather than TRF to b-tag jets. This takes account of the effect of fluctuations in the purities of the different b-tagged sub-samples and the b-tagging in general. The difference in the methods used for tagging provided the systematic uncertainty from this source.

Chapter 8

Results and Conclusions

8.1 Summary of the Results

We have presented a new precision measurement of the mass of the top quark using the Matrix Element method. The resolution of the measurement in the lepton+jets sample of $t\bar{t}$ condidates is enhanced by the application of a neural-net based b-tagging technique. The data set corresponds to ≈ 0.9 events/fb of integrated luminosity. The new developments in the method correspond to: (i) addition of an integration over electron resolution (previously only muon resolution was taken into the account). (ii) integration over transverse momentum of the $t\bar{t}$ system, which was neglected in the past. (iii) constraint of jet energies to the value derived from photon+jets data, with the mass of the W-boson providing a correction based on the $W \to q\bar{q}$ "hadronic" decay. (In the previous version of this analysis, the jet energy scale was set only in defining the hadronic W-boson mass.)

The combination of the e+jets and μ+jets channels in the analysis that ignores

b-tagging ("untagged") yields:

$$m_{\text{top}}(\text{untagged}) = 171.1 \pm 3.0(\text{stat} + \text{JES}) \pm 1.4(\text{syst}) \,\text{GeV}$$

$$= 171.1 \pm 3.3 \,\text{GeV} \tag{8.1}$$

The combination of the e+jets and μ+jets channels for the analysis where b-tagging information is used yields:

$$m_{\text{top}}(b{-}\text{tag}) = 170.5 \pm 2.4(\text{stat} + \text{JES}) \pm 1.2(\text{syst}) \,\text{GeV}$$

$$= 170.5 \pm 1.8(\text{stat}) \pm 1.6(\text{JES}) \pm 1.2(\text{syst}) \,\text{GeV}$$

$$= 170.5 \pm 2.7 \,\text{GeV} \tag{8.2}$$

All the steps we have taken have improved significantly the measurement of the mass of the top quark, and our result corresponds to the best measurement at DØ, and carries highest weight in the world average of $\approx 1\%$ precision.

8.1.1   Comparison to Previous Results

The former results based on 0.43 events/fb of integrated luminosity [53] (a factor of 2.1 of data less compared to the what was used in the present analysis) for the untagged and b-tagged analysis yielded:

$$m_{\text{top}}(\text{untagged}) = 169.2^{+5.0}_{-7.4}(\text{stat} + \text{JES}) \,\text{GeV}$$

$$m_{\text{top}}(b{-}\text{tag}) = 170.3^{+4.1}_{-4.5}(\text{stat} + \text{JES}) \,\text{GeV} \tag{8.3}$$

A comparison between the result given in Eq. 8.1 and the result in 8.3 shows that, on average, the uncertainty decreased by a factor equivalent to over a four-fold

increase in data.

For the b-tagged analysis, the comparison between the result in Eq. 8.3 and the result without using a JES prior (169.2 ± 2.7(stat + JES)) presented in the previous chapter, shows that the reduction on the uncertainty is better than expected, being equivalent to a factor of 2.5 increase in data. Implementing the prior, the increase in resolution is equivalent to a factor of 3.2 in data as seen when comparing Eq. 8.3 with Eq. 8.2. Consequently, we can conclude that the present analysis made substantive improvements, beyond just statistical accuracy.

8.1.2   Considerations For the Future

Without major improvements in the resolution of the present analysis, we can estimate to reach a statistical uncertainty of $\approx$1 GeV when the integrated luminosity in DØ reaches the 4 events/fb of integrated luminosity. At this point, certain important issues must be addressed in order to improve the precision of the measurement any further. We can divide these issues into three main categories:

(i) When the amount of collected $t\bar{t}$ data increases, the statistical uncertainty on the measurement of the mass of the top quark will be comparable to the systematic uncertainties $\approx$1 GeV. If we expect to have significant gain from the access to more data, then an extra effort should be directed to reduce the main sources of systematics uncertainties.

(ii) The assumptions and approximations used in the current analysis rely on corrections that are small compared to their uncertainties. However, as the resolution of the measurement improves as a result of more collected data, the probabilities for signal and background should be modified to describe the physical $t\bar{t}$ and background events more realistically. Examples of such modifications involve the inclusion of the gluon fusion term in $t\bar{t}$ production, more realistic angular resolution

for jets, accounting for b quark jets in the background probability and, probably most important, a better description of jet resolution via improved energy transfer functions.

(iii) At the 0.5% level of uncertainty in the top mass, several ambiguities will arise in the theoretical interpretation of the mass of the top quark, e.g., whether the measured quantity is the pole mass in the complex energy plane what should be interpreted as a higher-order corrected quantity that takes account of a shift in mass resulting from QCD gluon radiation [65, 66]. This is a topic currently in development, and will become more critical as the resolving power of the analysis improves.

For the LHC, the situation is different, expecting to have several order of magnitude more $t\bar{t}$ data, stastical uncertainties will be negligible and, the precision measurement of the mass of the top quark from the Tevatron can be used from the start as a means of calibrating the energy of jets at the LHC.

Appendix A

Optimizing the Operating Point of the b-tagger

The operating point used for the NN b-tagger in this analysis is 0.65, corresponding to the least restrictive approved i.e. "Medium" setting. In the future, a more optimal point should be considered. In this Appendix we include a study performed on data to try to extract an optimal point for future use. The data are not corrected for the response in mass and JES, and do not use the Gaussian prior for JES. We analyze some of the points given in Table 4.1: L4, L3 L2, OldLoose, Medium and Tight. The resulting uncertainties in the uncorrected fits are shown in Fig. A.1. The optimal point appears to be L3, for the case of 1+2 b-tags. Alternatively, the OldLoose operating point is optimal when considereding the entire data set (i.e, 0+1+2 b-tags). To complement this study, the same analysis should be performed on ensembles using MC events.
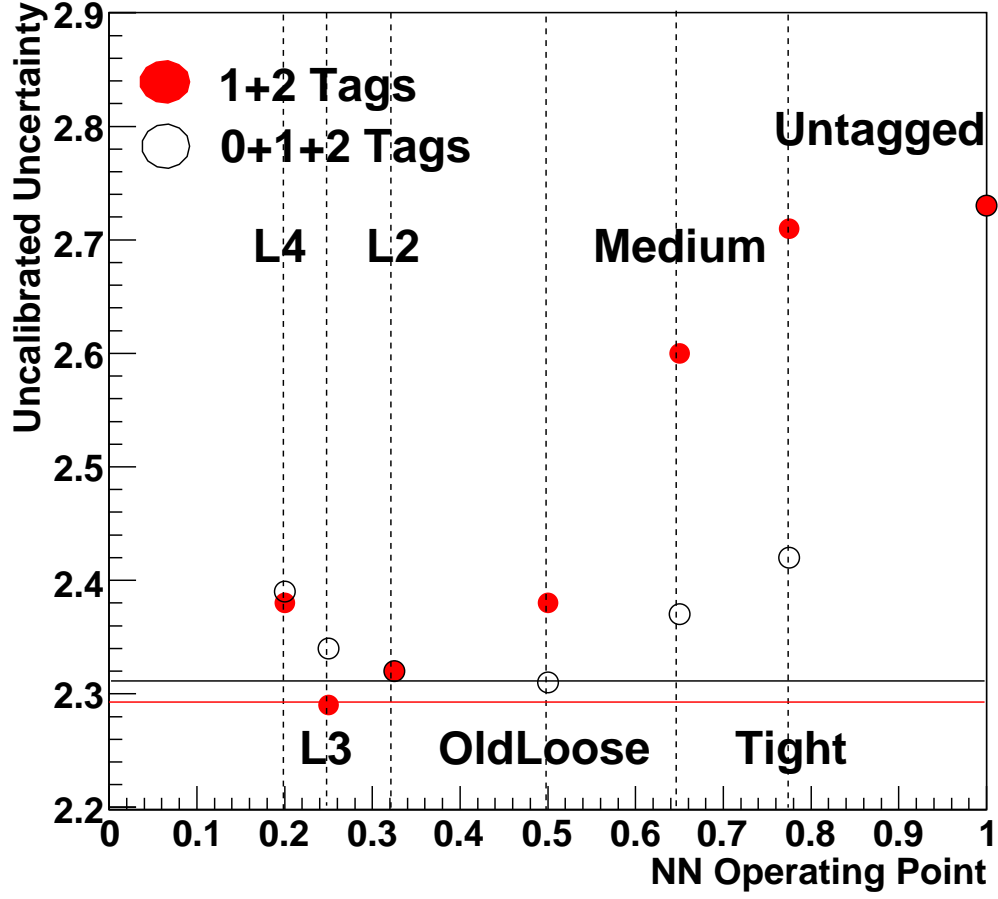
Figure A.1: The measured uncertainty for m_{top} in data as a function on the NN operating point for the b-tagged analysis for the 1+2 sample and for 0+1+2 sample of b-tagged events. The uncertainties are not inflated by the pull (uncorrected) which are assumed to be same for all operating points. The two horizontal lines show the minimun error achieved for the two types of samples. Also is shown for comparison the error when b-tagging is ignored (untagged) (this point at NN= 1 appears at the right-most part of the figure).

Bibliography

[1] CDF Collaboration, *Observation of the Top Quark in $p\bar{p}$ Collisions with the Collider Detector at Fermilab,* Phys. Rev. Lett. **74** , 2626 (1995).

[2] D0 Collaboration, *Observation of the Top Quark,* Phys. Rev. Lett. **74** , 2632 (1995).

[3] CDF Collaboration, *Study of $t\bar{t}$ Production in $p\bar{p}$ Collisions Using Total Transverse Energy,* Phys. Rev. Lett. **75** , 3997 (1995).

[4] CDF and DØ Collaborations, FERMILAB-CONF-01-095-E , (2001).

[5] M. J. G. Veltman, Physica **29** 186 (1963);
G. 't Hooft, *Gauge Field Theory* , in Proceedings of the Adriatic Meeting, Rovinj (1973), ed. M. Martinis et al., North Holland / Am. Elsevier, p.321.

[6] M. K. Gaillard, P. Grannis and F. J. Sciulli: *The Standard Model of Particle Physics,* Rev. Mod. Phys. **71** , 96-111 (1999).

[7] Particle Data Group Collaboration, Phys. Lett. **B** , 592 (2004).

[8] M. Gell-Mann, Phys. Lett. **8**, 214 (1964).

[9] G. Zweig, CERN reports No. 8182/TH.401 and No. 8419/TH. 412 (1964).

[10] P. W. Higgs, Phys. Rev. Lett. **12** , 132 (1964).

[11] P. W. Higgs, Phys. Rev. **145**, 1156 (1966).

[12] F. Englert and R. Brout: Phys. Rev. Lett. **13** , 321 (1964).

[13] G. S. Guralnik, C. R. Hagen and T. W. B. Kibble: Phys. Rev. Lett. **13** , 585 (1964).

[14] D. J. Gross and F. Wilczek, Phys. Rev. D **8** , 3633 (1973).

[15] ATLAS Collaboration, *Detector and physics performance technical design report,* CERN-LHCC-99-14 (1999).

[16] V.M. Abazov *et al.,* DØ Collaboration, *Evidence for production of single top quarks and first measurement of* $|V_{tb}|$, Phys. Rev. Lett. **98** , 181802 (2007)

[17] S. Weinberg, *The Quantum Theory of Fields Vol. I*, Cambridge University Press (2005).

[18] Accelerator Concepts Rookie Books, (2003).
http://www-bdnew.fnal.gov/operations/rookie_books/rbooks.html.

[19] DØ Collaboration, *The Upgraded DØDetector,* Nucl. Instr. and Meth. A **565**, 463 (2006)

[20] DØ Collaboration, *The DØ Upgrade,* FERMILAB-PUB-96/357-E (1996).

[21] DØ Collaboration, *The DØUpgrade, Central Tracker Technical Design Report.* (1999).
http://d0server1.fnal.gov/users/stefan/www/CFT_TDR/CFT_TDR.ps.

[22] V. Buescher, *Testing and characterization of VLPC cassettes,* DØ-Note 3912 (2001)

[23] L. Groers, *DØ Calorimeter Upgrades for Tevatron Run II,* DØ-Note 4240 Proceedings for the IXth International Conference on Calorimetry in Particle Physics, Annecy, France, Oct 9-14 (2000).

[24] Adams, M. *et al., Design Report of the Central Preshower Detector for the DØUpgrade* (1996). http://d0server1.fnal.gov/users/qianj/CPS/doc/dn3104.pdf.

[25] Gordeev, A. *et al., Technical Design Report of the Forward Preshower Detector for the DØUpgrade,* DØ Note 3445 (1998).

[26] T. Diehl *et al., Technical Design of the Cental Muon System,* DØ-Note 3365 (1998).

[27] T. Diehl *et al., Technical Design for the DØ Forward Muon Tracking Detector Based on Mini-Drift Tubes,* DØ-Note 3366 (1997).

[28] J. Brzenziak *et al.,* FERMILAB-TM-1886 (1994).

[29] M. Klute and A. Quadt, Measurements of Level 1 Trigger Efficiencies from DØ Data, DØ-Note 3949 (2002).

[30] T. Edwards *et al.,* FERMILAB-TM-2278-EB (2004).

[31] DØ Collaboration, *d0reco.* (2004). http://wwwd0.fnal.gov/Run2Physics/WWW/algorithm.htm.

[32] R. E. Kalman, J. Bas. Eng. D **82** , 35 (1960); R. E. Kalman and R. S. Brucy, J. Bas. Eng. D **83** , 95 (1961); P. Billoir, Nucl. Instr. Meth. A . **225** , 352 (1984).

[33] A. Schwartzman and C. Tully, *Primary Vertex Reconstruction by Means of Adaptive Vertex Fitting,* DØ-Note 4918 (2005).

[34] P. Calfayan *et al.*, *Muon Identification Certification for p17 data,* DØ-Note 5157 (2006).

[35] N. Gollub and L. Shabalina, *Measurement of the $t\bar{t}$ Production Cross Section at $\sqrt{s} = 1.96$ TeV in the μ+*jets Final State using a Topological Method on 363 pb^{-1} of PASS2 Data, DØ-Note 4954 (2005).

[36] J. Hays *et al.*, *Electron Likelihood Efficiency in p17 ,* DØ note 5114 (2006).

[37] G. Blazey *et al.*, *Run II Jet Physics,* DØ-Note 3750 (2000).

[38] Amnon Harel *Jet ID Optimization,* DØ-Note 4919 (2005).

[39] DØ Jet Energy Scale study group, *Jet Energy Scale at DØ RunII,* DØ-Note 4720 (2005).

[40] DØ Jet Energy Scale study group,
http://www-d0.fnal.gov/phys_id/jes/d0_private/certified/v5.3/links.html

[41] T. Scanlon, *A Neural Network b-Tagging Tool,* DØ-Note 4889 (2005).

[42] M. Anastasoaie *et al.*, *Performance of the NN b-Tagging Tool on p17 Data,* DØ-Note 5313 (2007).

[43] L. Chabalina *et al.*, Available at: `http://www-d0.fnal.gov/phys_id/bid/d0_private/certification/p14/CSIP/CSIP_v2.html`.

[44] D. Block *et al.*, *Performance of the JLIP b-tagger in p14,* DØ-Note 4348 (2004).

[45] L. Feligioni *et al.*, *Update on b-quark Jet Identification with Secondary Vertex Reconstruction using DØ Reco version p14,* DØ-Note 4414 (2004).

[46] V.M. Abazov *et al.* DØ Collaboration, *Measurement of the $t\bar{t}$ Production Cross Section at sqrt(s) = 1.96 TeV in Lepton+Jets Events using Topological Method on $1fb^{-1}$ of DØ data,* (approved October 2006). Available at: `http://www-d0.fnal.gov/Run2Physics/top/d0_private/` `top_private_web_pages/top_internal_review.html`.

[47] V.M. Abazov *et al.,* [DØ Collaboration], *Measurement of the $t\bar{t}$ Production Cross Section at sqrt(s) = 1.96 TeV in Lepton+Jets Events using Secondary Vertex B-tagging,* (under review for Moriond 2007). Available at: `http://www-d0.fnal.gov/Run2Physics/top/d0_private/top_` `private_web_pages/top_internal_review.html`.

[48] T. Sjostrand *et al.*, Comp. Phys. Commun. **135**, 238 (2001).

[49] M.L. Mangano et al., *ALPGEN, a Generator for Hard Multiparton Processes in Hadronic Collisions*, JHEP **307**, 1 (2003).

[50] V. M. Abazov *et al.*, DØ Collaboration, *Measurement of the $t\bar{t}$ Production Cross Section in ppbar Collisions at $\sqrt{s} = 1.96$ TeV Using Kinematic Characteristics of Lepton+Jets Events*, FERMILAB-PUB-05-079-E (Apr 2005), hep-ex/0504043.

[51] V.M. Abazov *et al.*, DØ Collaboration, *A precision measurement of the mass of the Top quark*, Nature **429**, 638 (2004).

[52] I. Volobouev, Private comunication.

[53] V.M. Abazov *et al.*. DØ Collaboration, *Measurement of the top quark mass in the lepton+jets final state with the matrix element method*, Phys. Rev. D **74**, 092005 (2006).

[54] F.A. Berends, H. Kuijf, B. Tausk, W.T. Giele, *On the Production of a W and Jets at Hadron Colliders*, Nucl. Phys. B **357**, 32 (1991).

[55] Private communication from L. Wang. Parameterization can found in the file: `/work/cole-clued0/leiwang/wz_epmcs/p170303_sampling/wz_epmcs/src/pmcsana.cpp`.

[56] E.T. Jaynes, *Probability Theory*, Cambridge University Press (2003).

[57] R. Field, *CDF Run2 Monte Carlo Tunes*. Available at: `www-cdf.fnal.gov/physics/conferences/cdf8547_RDF_Tev4LHC.pdf`.

[58] Y. Peters *et. al.*, *Factorizaton Scale, Estimate of Weights and Uncertainty*, Presentation given at DØ Top group meeting (2007).

[59] H. L. Lai *et al.*, CTEQ Collaboration, *Global QCD analysis of parton structure of the nucleon: CTEQ5 parton distributions*, Eur. Phys. J. C **12**, 375 (2000).

[60] J. Pumplin *et al.*, *New Generation of Parton Distributions with Uncertainties from Global QCD Analysis*, JHEP **207** , 12 (2002).

[61] M.G. Bowler, *e+ e- Production of Heavy Quarks in the String Model.*, Z. Phys C **11** , 169 (1981).

[62] C. Peterson *et. al*, *Scaling Violations in Inclusive e+ e- Annihilation Spectra*, Phys. Rev. D **27**, 105 (1983).

[63] Y. Peters *et. al.*, *Reweighting of the Fragmentation Function for the DØ Monte Carlo*, DØ Note 5325 (2007).

[64] The ALEPH, DELPHI, L3, OPAL, and SLD Collaborations, the LEP Electroweak Working Group, SLD Electroweak Group, and SLD Heavy Flavour

Group, *Precision Electroweak Measurements on the Z Resonance*, SLAC-R-774 (2005), hep-ex/0509008.

[65] S. Fleming *et. al*, *Jets from Massive Unstable Particles: Top-Mass Determination* (2007), hep-ph/0703207.

[66] P. Skands *et. al*, *Non-perturbative QCD Effects and the Top Mass at the Tevatron*, FERMILAB-PUB-06-340-T (2007), hep-ph/0703081.